Assessing the effects of forest health on sun-induced chlorophyll fluorescence using the FluorFLIGHT 3-D radiative transfer model to account for forest structure

R. Hernández-Clemente[1*], P.R.J. North[1], A. Hornero[2], P.J. Zarco-Tejada[3]

[1] Department of Geography, Swansea University, SA2 8PP, Swansea, UK.
[2] Instituto de Agricultura Sostenible (IAS), Consejo Superior de Investigaciones Científicas (CSIC), Córdoba, Spain
[3]European Commission, Joint Research Centre (JRC), Directorate D – Sustainable Resources - Bio-Economy Unit, Via E. Fermi 2749 – TP 261, 26a/043, I-21027 Ispra (VA), Italy

*Corresponding author:

Rocío Hernández Clemente
Department of Geography
Swansea University
SA2 8PP- Swansea,
UK
Tel: +44 1792 295860
Fax: +44 1792 295110
e-mail: r.hernandez-clemente@swansea.ac.uk
http://orcid.org/0000-0002-4434-8346

Submitted to *Remote Sensing of Environment*
August 2016

Abstract

Sun-induced fluorescence (SIF) has been proven to serve as a proxy of photosynthesis activity and therefore, as an early indicator of physiological alterations for global monitoring of vegetation. However, the interpretation of SIF over different spatial resolutions is critical to bridge the existing gap between local and global scales. This study provides insight into the influence of scene components, and forest structure and composition on the quantification of the red and far-red fluorescence signal as an early indicator of forest decline. The experiments were conducted over an oak forest (*Quercus ilex*) affected by water stress and *Phytophthora* infection in the southwest of Spain. SIF retrievals through the Fraunhofer Line Depth (FLD) principle with three spectral bands F (FLD3) was assessed using high resolution (60 cm) hyperspectral imagery extracting sunlit crown, full crown and aggregated pixels. Results showed the link between F (FLD3) extracted from sunlit crown pixels and the tree physiological condition in this context of disease infection, yielding significant relationships (r^2=0.57, p<0.01) for midday xylem water potential (ψ), (r^2=0.63, p<0.001) for the de-epoxidation state of the xanthophyll cycle (DEPS), and (r^2=0.74, p<0.001) for leaf-level measurements of steady-state fluorescence yield (F_s). In contrast, a poor relationship was obtained when using aggregated pixels at 30 m spatial resolution, where the relationship between the image-based F (FLD3) and F_s yielded a non-significant relationship (r^2=0.25, p>0.05). These results demonstrate the need for methods to accurately retrieve crown SIF from aggregated pixels in heterogeneous forest canopies with large physiological variability among individual trees. This aspect is critical where structural canopy variations and the direct influence of background and shadows affect the SIF amplitude masking the natural variations caused by physiological condition. FluorFLIGHT, a modified version of the three dimensional (3-D) radiative transfer model FLIGHT was developed for this work, enabling the simulation of canopy radiance and reflectance including fluorescence at different spatial

resolutions, such as may be derived from proposed satellite missions such as FLEX, and accounting for canopy structure and varying percentage cover. The 3-D modelling approach proposed here significantly improved the relationship between F_s and F (FLD3) extracted from aggregated pixels (r^2=0.70, p<0.001), performing better than when aggregation effects were not considered (r^2=0.42, p<0.01). The FluorFLIGHT model used in this study improved the retrieval of SIF from aggregated pixels as a function of fractional cover, leaf area index and chlorophyll content yielding significant relationships between F_s ground-data measurements and fluorescence quantum yield estimated with FluorFLIGHT at p<0.01 (r^2=0.79). The methodology presented here using FluorFLIGHT also demonstrated its capabilities for mapping SIF at the tree level for single tree assessment of forest physiological condition in the context of early disease detection.

Keywords

Fluorescence, stress detection, hyperspectral, SIF, RTM, forest dieback, oak forest, *Phytophthora* infection.

1. Introduction

Spatial and temporal estimation of photosynthesis of forest ecosystems can provide advance information on plant performance and forest dynamics in a given environment. Sun-induced chlorophyll fluorescence (SIF) has been extensively tested as a proxy of fundamental processes of plant physiology to understand the photosynthetic activity of plants and the stress development affecting photochemistry (Damm et al., 2014; Krause and Weis, 1984; Zarco-Tejada et al., 2013a). Current research efforts to monitor photosynthetic activity show a growing interest in remote sensing of the SIF signal due to its potential to be measured at

both local (high resolution images) and global scales (medium and low resolution images) being a direct proxy of photosynthesis. The first global maps of SIF were published (Frankenberg et al., 2011; Joiner et al., 2014) using the TANSO sensor on board GOSAT (Kuze et al., 2009) allowing qualitative assessments with annual and seasonal vegetation patterns (Guanter et al., 2012). The spatial resolution provided by this sensor (10.5 km) is not, however, sufficient for the understanding of the retrieved SIF in heterogeneous vegetation canopies due to the aggregation of scene components and the large effects caused by background and shadows (Zarco-Tejada et al., 2013b). The fast development of new hyperspectral sensors to be carried on board manned and unmanned airborne platforms has given rise to the retrieval of high spatial resolution SIF at local scales, which is becoming a novel area of research (Damm et al., 2015; Zarco-Tejada et al., 2013c). However it remains very challenging to cover at very high resolution the large areas required for forest monitoring analysis. This has hitherto been the main limitation in studying physiological condition of forest canopies with higher detail, as currently available satellite sensors are limited by their spatial and spectral resolution for SIF retrieval purposes. To address this gap, the ESA's Earth Explorer Mission of the 'Fluorescence Explorer' (FLEX) (Kraft et al., 2012), the first mission designed to observe the photosynthetic activity of the vegetation layer has been recently approved, with 2022 as the tentative launch date. This mission will make possible, for the first time, the assessment of the dynamics of photosynthesis on forest canopies through SIF at 300 m spatial resolution, and with potential to distinguish different fluorescence signals from PSI and PSII (Rossini et al., 2015). This offers a great advantage over current techniques used for photosynthesis monitoring based on structural indices (e.g. the Normalized Difference Vegetation Index (NDVI)) acquired from conventional Earth-resource satellites.

105 The chlorophyll fluorescence signal derived from global maps is affected by illumination
106 effects, leaf and canopy structure and composition of vegetation, and soil / background
107 though to a lesser extent than reflectance. The interplay of within-leaf scattering properties of
108 leaf structure and biochemical constituents are known to affect the bidirectional chlorophyll
109 fluorescence emission (Van Wittenberghe et al., 2015, 2014; Verrelst et al., 2015). SIF flux
110 through a leaf, upward and downward leaf chlorophyl fluorescence emissions and scattering
111 effects have been thoroughly studied using radiative transfer models (RTMs) (Miller, 2005).
112 However, few fluorescence models have been developed at the leaf level and even fewer are
113 available at the canopy level, especially for the case of heterogeneous and complex canopies.
114 The first attempts were carried as part of a vegetation fluorescence canopy model developed
115 in the framework of the ESTEC ESA project (16365/02/NL/FF). The FluorMODleaf (Pedrós
116 et al., 2008) and FluorSAIL (Verhoef, 2004) leaf and canopy fluorescence models were
117 developed within the same project. FluorMODleaf is based on the widely used and validated
118 PROSPECT leaf optical properties model and requires inputs from PROSPECT-5 plus the
119 $\sigma II/\sigma I$ ratio referring to the relative absorption cross-sections of PSI and PSII, as well as the
120 fluorescence quantum efficiency of PSI and PSII, represented by the corresponding mean
121 fluorescence lifetimes τI and τII. The canopy model is based on the turbid medium SAIL
122 model (FluorSAIL) coupled with FluorMODleaf and MODTRAN to provide the illumination
123 levels through the canopy. The Soil Canopy Observation, Photochemistry and Energy fluxes
124 (SCOPE) model recently developed by van der Tol et al., (2009) as a means of jointly
125 simulating directional Top of Canopy (TOC) reflected solar radiation, emitted thermal
126 radiation and SIF signals as well as energy balance, water and CO_2 fluxes, enables vertical
127 (1-D) modelling of integrated radiative transfer and energy balance by combining a number
128 of intra-canopy radiative, turbulent and mass-transfer models, bearing in mind various
129 processes involved in leaf biochemistry (Duffour et al., 2015). Using retrievals of SIF

simulated with SCOPE, Verrelst et al. (2015) demonstrated that the main variables affecting SIF signal were determined by leaf optical properties and canopy structural variables with a contribution of 77.9% of the SIF total variability. Canopy re-absorption and scattering effects must be better understood and quantified. Consequently, it is very important to make progress on canopy-scale modelling approaches providing an explicit connection between the canopy biophysical processes, view and illumination geometry and the resulting canopy fluorescence signal. In light of the above, Zarco-Tejada et al. (2013b) demonstrated the need for RTM methods to accurately retrieve vegetation fluorescence signal from vegetation-soil/background aggregated pixels. Due to the lack of complex models to simulate SIF in heterogeneous canopies, Zarco-Tejada and co-authors conducted the study using a leaf-canopy fluorescence model (FluorMODleaf) combined with a geometric model to account for canopy heterogeneity (FluorSAIL) and a first-order approximation forest model (FLIM) of stand reflectance to account the effects of crown transparency and shadowing on apparent reflectance. The results demonstrated the large structural effects on the fluorescence retrieval from mixed pixels, and therefore the need to develop more complex models to account for the effect caused by the canopy architecture.

This aspect becomes particularly important in the assessment of complex forest canopies characterised by high horizontal and vertical heterogeneity (Widlowski et al., 2015). Unfortunately, currently available fluorescence models are only valid on homogeneous and uniform canopies. Strategies to simulate the spectral signature in heterogeneous forest canopies have been limited by difficulties in simulating canopy structure such as Leaf Area Index (LAI), tree density, fractional cover (FC), crown overlapping or mutual shading and multiple scattering between crowns. This paper aims to fill these gaps and in doing so to assess the potential of chlorophyll fluorescence signal retrieval as an early indicator of forest decline. The novel approach consists of coupling the leaf optical model FLUSPECT (Vilfana

et al., 2016) and the three-dimensional (3-D) ray-tracing model FLIGHT developed by North, (1996) to carry the scaling up approach from leaf to canopy dealing with multiple canopy components. In particular, the study aims at assessing: i) SIF as an early indicator of forest health in a heterogeneous oak forest canopy (*Quercus ilex*) affected by water stress and *Phytophthora* infection using very high resolution airborne hyperspectral imagery, ii) the canopy structure effects on the retrieval of SIF in forest canopies using a 3-D RTM, and iii) the retrieval of SIF through model inversion using coarse-spatial resolution hyperspectral imagery.

2. Materials and methods.

The methods used for the assessment of SIF from hyperspectral imagery for the early detection of forest decline condition are described below, outlining field and airborne data collection, as well as the approach using the 3-D RTM FLIGHT adapted to account for fluorescence (FluorFLIGHT). In both cases, SIF was retrieved within the far-red region.

2.1. Field data collection.

The experimental area is located in Puebla de Guzmán (Huelva province, in southwestern Spain) (Lat 37°36'30.89"N, Lon 7°20'27.97"W) (Fig. 1). The topography is slightly hilly, with acidic and poor soils. The annual rainfall is around 490 mm with an annual average temperature of 18.1 °C, reaching an annual average of 32 °C during summer and an annual average of 12.7 °C during winter. The vegetation is mainly composed of mature trees of the species *Quercus ilex* subsp. Bellota with an average density of 60 trees per ha (Roig Gómez et al., 2007). Since the 1990s, trees have shown symptoms of decline, leading to high mortality rates from the 2000s (Maurel et al., 2001). This region is particularly vulnerable because of the combined effect of water deficiency, soil compaction, nutrient losses, water

erosion and the widespread distribution of soil-borne pathogen (*Pytophthora cinnamomi* and *Pythiumspiculum*) (Moralejo et al., 2009).

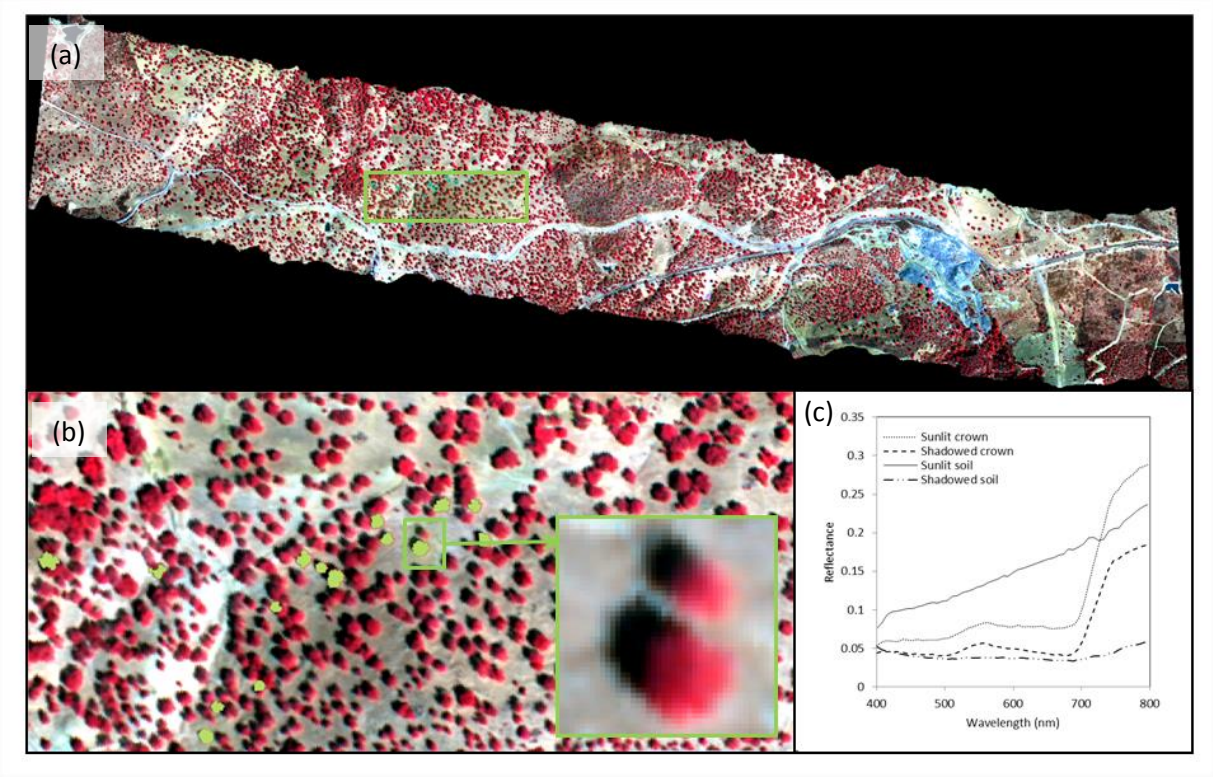

Fig. 1. Airborne hyperspectral flight line acquired with the micro-hyperspectral imager yielding 60 cm resolution (a), oak forest study site and tree crowns selected for the quantification of SIF (b), high resolution spectral reflectance extracted from sunlit and shadowed crown and soil components (c).

The field data measurements were conducted in 15 oak trees (*Quercus ilex* subsp. Bellota) with similar height and age located in low slope areas (< 10%). The location of these trees was previously associated with the pathogenicity of *P. cinmaomi* (Ferraz et al., 2000) and heat-induced tree die-off processes (Natalini et al., 2016). The trees were selected to ensure a gradient in health condition based on the physiological variables: de-epoxidation of the xanthophyll cycle (DEPS), midday xylem water potential (ψ) and steady-state fluorescence yield (F_s). Three different forest physiological conditions (FPC-1,2,3) were established based

194 on these variables, where FPC1 correspond with the healthier and more vigorous trees, FPC2
195 with moderated affected trees, and FPC3 with declining trees. In order to determine whether
196 FPCs differed significantly in terms of DEPS, ψ and Fs, a one-way ANOVA was performed
197 at a 0.05 significance level. Findings indicated significant differences in physiological status
198 for each FPC ($p < 0.05$). A similar procedure was used by Hernández-Clemente et al. (2011)
199 to established physiological condition levels in a conifer forest affected by water stress.

200 A summary of the variables measured in the field is included in Table 1. Physiological
201 measurements were carried out concurrently with the airborne measurements (12:00 to 13:00
202 h local time) during three consecutive days (25-28 August in 2012). ψ was measured with a
203 pressure chamber (SKPM 1400, Skye Instruments Ltd, Powys, UK) (Scholander et al., 1965)
204 from 12 branches per tree, three branches per orientation in the four cardinal directions. F_s
205 was measured on five leaves per orientation and tree, with a total of 300 leaves sampled. Leaf
206 fluorescence was measured using a FluorPen FP100 (Photon Systems Instruments, Brno,
207 Czech Republic), which was self-calibrated at the start of each session. Although
208 measurements made with the FluorPen FP100 differed from airborne SIF retrievals, leaf data
209 served as a field-level assessment of variability in stress conditions (Zarco-Tejada et al.,
210 2016).

211 Leaf biochemical constituents measured from the selected trees were total chlorophyll (C_{a+b})
212 (chlorophyll a (C_a) and chlorophyll b (C_b)), total carotenoids (C_{x+c}) and xanthophyll
213 pigments, and leaf water content (C_w) and dry mass (C_s). Leaf-level measurements were
214 collected on a total of 48 leaves per tree, 12 samples per orientation, with a total of 720 leaves
215 sampled. The samples were collected from the top of the crown by selecting branches of
216 illuminated areas. Leaf pigments were processed and extracted as reported by Hernandez-
217 Clemente et al. (2011). The DEPS was calculated as (A+Z)/(A+V+Z) (Thayer & Björkman,
218 1990), where V is violaxanthin, A is antheraxanthin and Z is zeaxanthin.

Optical measurements were taken on leaves from the same branches and trees used for pigment quantification. Leaf reflectance (ρ) and transmittance (τ) were measured with a Li-Cor 1800-12 integrating sphere (Li-Cor, Lincoln, NE, USA) coupled to a fiber optic spectrometer (Ocean Optics model USB2000 spectrometer, Ocean Optics, Dunedin, FL, USA), with a 1024-element detector array, 0.5 nm sampling interval, and 7.5 nm spectral resolution in the 340–940 nm range using the method described in Zarco-Tejada et al. (2005).

Table 1.

Ground truth data collected and optical measurements.

Variable	Symbol	Units
Biochemical constituents & physiological variables		
Chlorophyll content	C_{a+b}	$\mu g/cm^2$
Carotenoid content	C_{x+c}	$\mu g/cm^2$
Water content	C_w	mg/cm^2
Dry matter	C_m	mg/cm^2
Xanthophyll cycle	DEPS	arbitrary units
Steady State Fluorescence	Fs	arbitrary units
Water potential	ψ	mpa
Optical measurements		
Leaf reflectance	ρ	%
Leaf transmittance	τ	%
Solar irradiance	Io	$wm^{-2}sr^{-1}nm^{-1}$
Forest canopy structure		
Density	D	trees/ha
Trunck diameter	Øt	m
Tree height	H	m
Crown diameter	$Ø_c$	m
Crown heigtht	H_c	m
Leaf Area Index	LAI	m^2/m^2

In February 2013, the study area was inventoried recording the main structural variables of the canopy. A total of 200 trees were measured recoding the trunk diameter at 1.3 m, tree height, crown diameter, tree density, FC and height. Additionally, LAI values were taken

from a subsample of 15 trees of this data set. A detailed description of the measurement procedure can be found in Hernandez-Clemente et al. (2014).

2.2. Airborne image acquisitions

The airborne campaign was conducted with a hyperspectral sensor installed on an aircraft (CESSNA C172S EC-JYN) operated by the Laboratory for Research Methods in Quantitative Remote Sensing (QuantaLab), Consejo Superior de Investigaciones Científicas (IAS-CSIC, Spain) at 650-700 m above ground level (AGL) and 2800 ft. above the sea level (ASL). The images were acquired concurrent with field data acquisitions on 28 August 2012 between 11:30 and 13:00, local time.

The images were collected with a visible and near-infrared (VNIR) micro-hyperspectral imager (Micro-Hyperspec VNIR model, Headwall Photonics, MA, USA). The sensor was configured in the spectral mode of 260 bands at 1.85 nm/pixel and 12-bit radiometric resolution and radiometrically calibrated as described in Zarco-Tejada et al. (2013c). The hyperspectral sensor flown on board a manned platform yielding a 6.4 nm full-width at half-maximum (FWHM) with a 25-micron slit in the 400–885 nm region and 60 cm pixel size (Fig. 1). Data acquisition and storage module achieved a 50 fps (frames per second) with 18-ms integration time. The 8-mm optical focal length lens yielded an instantaneous field of view (IFOV) of 0.93 mrad and an angular field of view (FOV) of 49.82°. Radiance values were converted to reflectance using total incoming irradiance measured at the time of image acquisition. Field measurements were taken with an ASD Field Spectrometer (FieldSpec Handheld Pro, ASD Inc, CO, USA) with a cosine corrector-diffuser probe for the 350-1050 nm spectral range at lower resolution (3 nm FWHM). The ASD Field Spectrometer was first calibrated using a Spectralon (SRT-99-180, Labsphere, NH, USA) white panel. ASD measurements were resampled to 6.5 nm by Gaussian convolution to match the irradiance

spectra to the spectral resolution of the radiance imagery acquired by the hyperspectral airborne sensor.

The high resolution hyperspectral imagery (Fig. 1a) acquired over the oak forest (Fig. 1b) enabled the identification of different scene components (Fig. 1c) for field validation purposes. The fluorescence signal was quantified using the 760-nm O_2-A in-filling method based on the Fraunhofer line depth (FLD) calculated from a total of three bands (FLD3):

$$F = \frac{E_{out} * L_{in} - E_{in} L_{out}}{E_{out} - E_{in}} \quad (1)$$

where radiance, L, corresponds to L_{in} (L761), L_{out} (average of L747 and L780 bands), and the irradiance, E, to E_{in} (E761), and E_{out} (average of E747 and E780 bands).

Other vegetation indices mostly related with physiology such as the Photochemical Reflectance Index (PRI) (Gamon et al., 1992) and the Red Edge ratio index (RE) (Zarco-Tejada et al., 2001) and with canopy structure such as the NDVI (Rouse et al., 1972) were also tested in this study.

The hyperspectral imagery acquired enabled full crown pixels identification (Fig. 2a) and shaded and sunlit components within each crown (Fig. 2b). Thus, in order to assess the implications of scene components on the SIF signal when quantified in large pixels, FLD was quantified from three different strategies of aggregation (Fig. 2): from only sunlit pixels within each crown, all pixels from each tree crown (full crown pixels, including shaded and sunlit pixels) and from aggregated pixels at 30x30 m (including tree crown, bare soil and shadows).

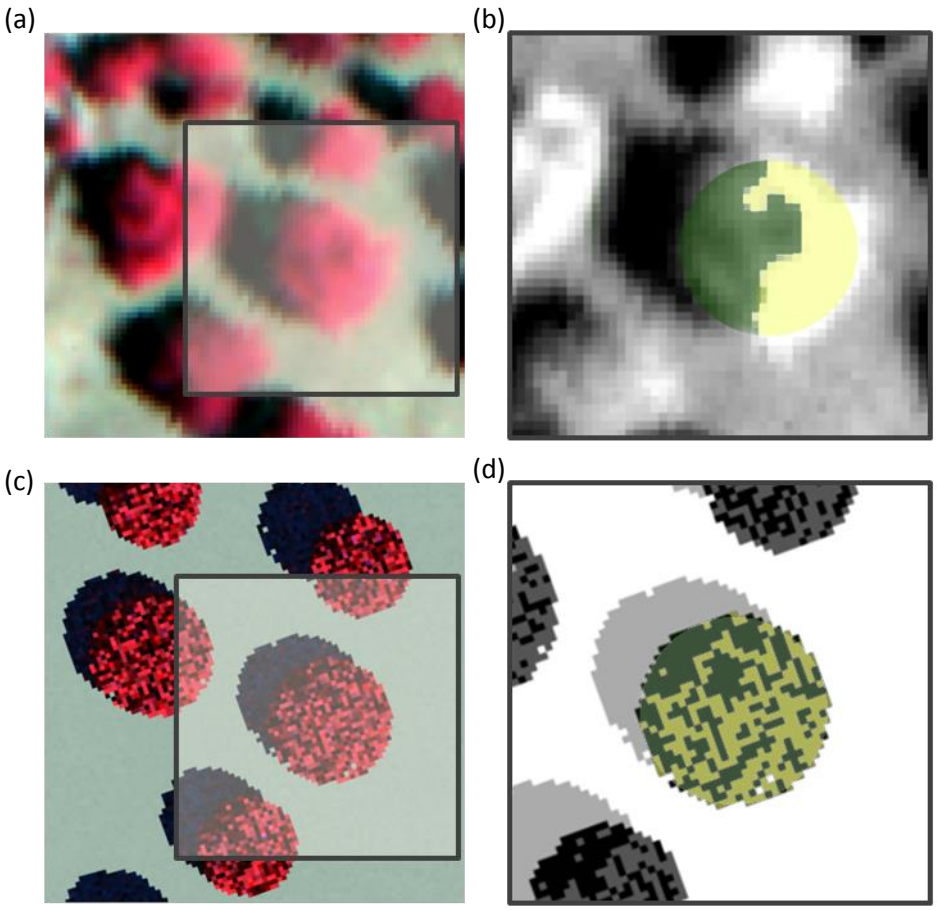

Fig. 2. Example of a 30x30 m scene (highlighted squared) of the micro-hyperspectral imagery acquired at 40 cm resolution in color-infrared (a) and sunlit and shadowed component identification of the crown on the micro-hyperspectral imagery (b). Example of a 30x30 m scene (highlighted squared) simulated with FluorFLIGHT (c) and sunlit and shadowed component identification on simulated images (d).

2.3. FluorFLIGHT model

FluorFLIGHT is a 3-D integrated RTM to calculate reflectance and fluorescence in the observation direction as a function of canopy components. It is based on existing theory of radiative transfer by coupling the leaf fluorescence model FLUSPECT and the 3-D ray-tracing model FLIGHT to account for canopy heterogeneity. The FluorFLIGHT model was specifically developed to assess the sensitivity of the fluorescence signal on heterogeneous forest canopy images.

FLUSPECT model is based on the Kubelka-Munk equation and requires a total of 7 inputs included in Table 2. Six of them are original parameters from the PROSPECT model (Feret et al., 2008; Jacquemoud and Baret, 1990), i.e., leaf structure parameter N, chlorophyll a+b (C_{a+b}) and carotenoid (C_{c+x}) content, water equivalent thickness in cm (C_w), dry matter content (C_m) and the senescence material (C_s). An additional parameter, the fluorescence quantum efficiency (F_i), from 0 (no fluorescence) to 0.1 (10% fluorescence), is required to calculate the excitation-fluorescence matrix for each photosystem (PSI and PSII). For this study, the F_i of PSI was fixed at one-fifth that of PSII, as the total spectrally integrated flux of PSII has been reported to be typically fivefold that of PSI (Franck et al., 2002). The FLUSPECT model generates two excitation-emission fluorescence matrices (EEFM) from 640-850 nm at 1 nm resolution and the reflectance and transmittance spectra of a leaf from 400-850 nm at 1 nm resolution. The EEFM matrices are separately generated for each photosystem for both sides of the leaf -the illuminated and the shaded side of the leaf-, backward and forward scattering matrices, respectively.

The FLIGHT model is based on Monte Carlo and deterministic ray tracing techniques to simulate the observed reflectance response of 3-D vegetation canopies (North, 1996, North et al., 2010). Multiple scattering within crown boundaries and between the crowns and other canopy components is modelled to account for canopy heterogeneity. It has formed one of a set of six benchmark models for RTM evaluation under the RTM Intercomparison (RAMI) project (Widlowski et al., 2008, 2007). Structural data may be specified as a statistical distribution, derived from field measurements or by direct inversion from lidar data (Bye et al., 2017). FLIGHT calculates directional reflectance by accumulating photon energy in the observation direction as a function of different forest canopy components defining the canopy structure (crown shape and size, tree height, position, density and distribution) (Table 2). The

distribution and absorption of light intercepting the canopy was calculated with a modified version of FLIGHT including the EEFM contribution to radiance.

Table 2.

Nominal values and range of variation used in FluorFLIGHT simulation analysis based on field data measurements.

Variable	Variable code	Nominal values	Range
FLUSPECT			
Mesophyll structure	N	2.1	-
Chlorophyll content	C_{a+b} (µg/cm^2)	35	10-60
Carotenoid content	C_{x+c} (µg/cm^2)	12	5-20
Water content	C_w (mg/cm^2)	0.013	-
Dry matter	C_{dm} (mg/cm^2)	0.024	-
Senescent material	C_s	0	0
Fluorescence quantum efficiency	F_i	0.04	0-0.1
FLIGHT			
Solar zenith, view zenith (º)	$\theta_{s,}$ θ_v	31.3, 0.0	-
Solar azimuth, view azimuth (º)	Φ_s, Φ_v	30.44, 0.0	-
Total LAI		3.15	0-3
Leaf angle distribution	LAD[1-9]	0.015, 0.045, 0.074, 0.1,0.123, 0.143, 0.158,0.168, 0.174	
Fractional cover (%)	FC	70	0-100
Crowns shape	CSh	ellipsoid	
Crown coordinates, radius, and centre to top distance	$X_{i,}$ Y_i, E_{xy}, E_z (m)	6.0, 5.0	
Minimum and Maximum height to first branch (m)	Hmin, Hmax	4.0, 10.0	
Density (trees/ha)	D	60	8-400
Soil reflectance	$\rho_{\lambda soil}$	ASD measurements	
Soil roughness	Θ_{soil}	0	
Solar irradiance	$\rho_{\lambda s}$	ASD measurements	

In addition, the canopy model requires a soil spectrum, solar irradiance (inputs from Table 2) and the six outputs obtained from the leaf model: leaf reflectance without fluorescence (ρ_n), leaf transmittance without fluorescence (τ_n), and the backward and forward fluorescence matrices for each photosystem (MbI, MbII, MfI, MfII).

Within FLIGHT, illumination at a facet such as a leaf is calculated as the sum of direct and diffuse incoming light. For a facet L with normal vector Ω_L, viewed from vector direction Ω_m and illuminated from vector direction Ω_0, the surface-leaving radiance contribution to the detector excluding fluorescence is defined according to the equation:

$$I_L(\lambda) = I_0(\lambda)\gamma_L(\Omega_0 \to \Omega)P_0 + \frac{1}{m}\sum_1^m I_m(\lambda)(\Omega_m)\gamma_L(\Omega_m \to \Omega) \qquad (2)$$

Where I_0 is the direct solar beam illumination radiance at wavelength λ, and I_m denotes a sample of the incoming diffuse field from direction Ω_m, and γ_L is the bi-directional reflectance or transmittance factor for facet L. P_0 has value 1 if there is a direct path to the source illumination, and 0 otherwise.

The non-fluorescent scattering contribution for an individual facet L at wavelength λ is approximated here using a bi-Lambertian reflectance/transmittance model:

$$\gamma_L(\Omega_L, \Omega' \to \Omega) = \begin{cases} \pi^{-1}\rho_n(\lambda)|\Omega \cdot \Omega_L|, if\ (\Omega \cdot \Omega_L)(\Omega' \cdot \Omega_L) < 0 \\ \pi^{-1}\tau_n(\lambda)|\Omega \cdot \Omega_L|, if\ (\Omega \cdot \Omega_L)(\Omega' \cdot \Omega_L) > 0 \end{cases} \qquad (3)$$

The fluorescence contribution F_L is calculated using similar equations, but using the full fluorescent scattering matrices at leaf level, sampling direct and diffuse leaf-level incident illumination within the excitation range 400-750 nm:

$$F_L(\lambda) = \sum_{k=400}^{750} \left(I_0(k)\gamma_F(\Omega_0 \rightarrow \Omega)P_0 + \frac{1}{m}\sum_1^m I_m(k)(\Omega_m)\gamma_F(\Omega_m \rightarrow \Omega) \right) \quad (4)$$

where

$$g_F(W_L, W' \rightarrow W) = \begin{Bmatrix} \rho^{-1} Mb[k, l]|W \cdot W_L|, if\ (W \cdot W_L)(W' \cdot W_L) < 0 \\ \rho^{-1} Mf[k, l]|W \cdot W_L|, if\ (W \cdot W_L)(W' \cdot W_L) > 0 \end{Bmatrix} \quad (5)$$

Where *Mb* is the sum of backward scattering matrices for PSI and PSII contributions, and *Mf* for forward scattering. Total measured radiance is calculated as the sum of the reflected light and fluorescent emission terms. The full evaluation of the fluorescence scattering matrices at each photon interaction at leaf level allows inclusion of fluorescent emission in TOC spectra, accounting for 3-D structure, multiple scattering, and leaf-level light environment. Furthermore, the simulated reflectance at the canopy level accounts for crown overlapping, mutual shading, and multiple scattering among crowns. Sunlit and shadowed pixels of the crown are identified based on the scene components mask derived from the FluorFLIGHT model simulations (Fig. 2c, d). This makes it possible to understand the contribution of each component at different resolutions, particularly important for sensors acquiring data with lower spatial resolutions and therefore, with higher aggregation effects (Fig. 3). As an example, the fluorescence peak experimentally observed in canopy reflectance and simulated with FluorFLIGHT can be shown in (Fig. 3a, b).

The model is originally developed at 1 nm FWHM. Nevertheless, for comparisons against the airborne hyperspectral imagery, the model simulations are convolved to 6.5 nm FWHM to match the spectral resolution of the radiance imagery acquired by the hyperspectral airborne sensor. If no convolution is carried, the FWHM of the 1 nm (model) vs 6.5 nm (image) would

derive different levels of fluorescence emission. Accounting for the bandwidth of the imagery enables the comparison between the fluorescence retrieved from the model and the one retrieved from the image at the tree crown level.

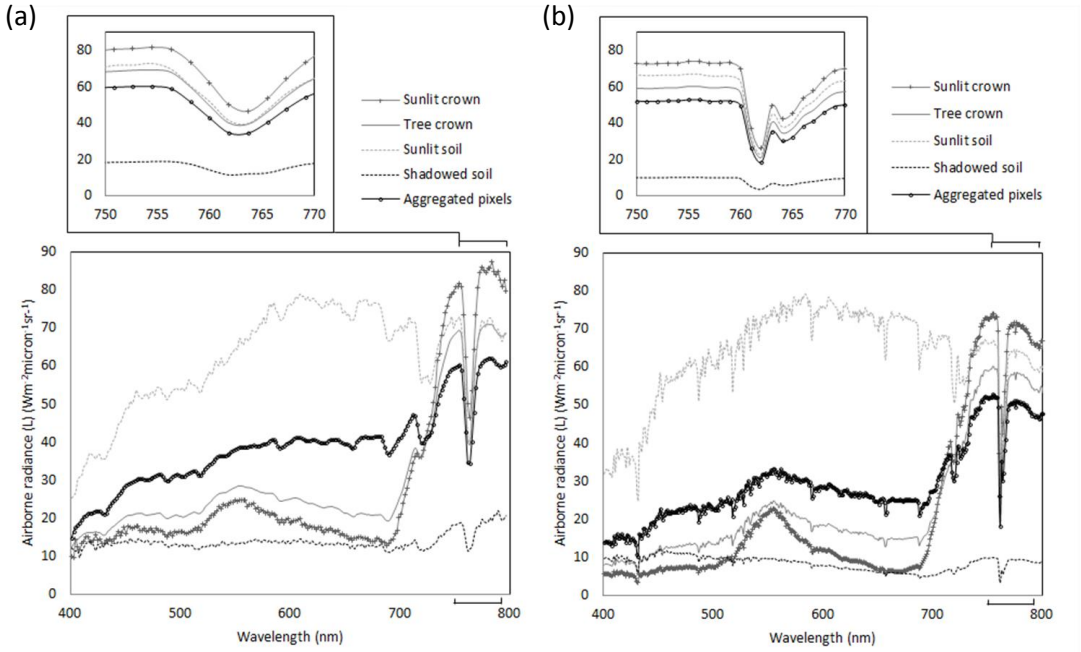

Fig. 3. Example of the spectral radiance extracted from the micro-hyperspectral image (a) and from FluorFLIGHT simulated radiance (L) (b) for different scene componens: sunlit crown, full crown, sunlit soil, shadowed soil and aggregated pixels (30x30 m) in the O_2-A feature used for fluorescence quantification. Spectral features extracted from Fig. 2.

2.4. Model simulation approach

The coupled 3-D fluorescence model FluorFLIGHT was used in this study with two primary objectives: i) the analysis of forest structure effects on SIF retrievals at high resolution scale, ii) the estimation of SIF from coarse-spatial-resolution imagery by Look-Up Table (LUT-based) model inversion to account for the canopy architecture.

i) Modelling forest canopy structural effects on fluorescence signal.

FluorFLIGHT was used to analyse the variation of SIF as a function of forest structural components. The aim of this analysis was to assess the influence of scene components on the

retrieval of the chlorophyll fluorescence signal by identifying the key variables determining SIF variations at different scales. To do this, SIF was quantified using the 760-nm O_2-A in-filling method (FLD3) from FluorFLIGHT simulated data from three different strategies of aggregation (Fig. 2): from only sunlit pixels within each crown, all pixels from each tree crown and from aggregated pixels at 30x30 m (including tree crown, bare soil and shadows). This selection was based on the SIF variations found over different levels of aggregation in both, imagery and simulated spectra (Fig. 4). Fig. 4 shows the variation in SIF extracted from the original high-resolution airborne hyperspectral image (Fig. 4c) and from a FluorFLIGHT image (Fig. 4d) as a result of increasing the pixel-aggregation level from sunlit crown pixels to aggregated pixels of 100x100 m window.

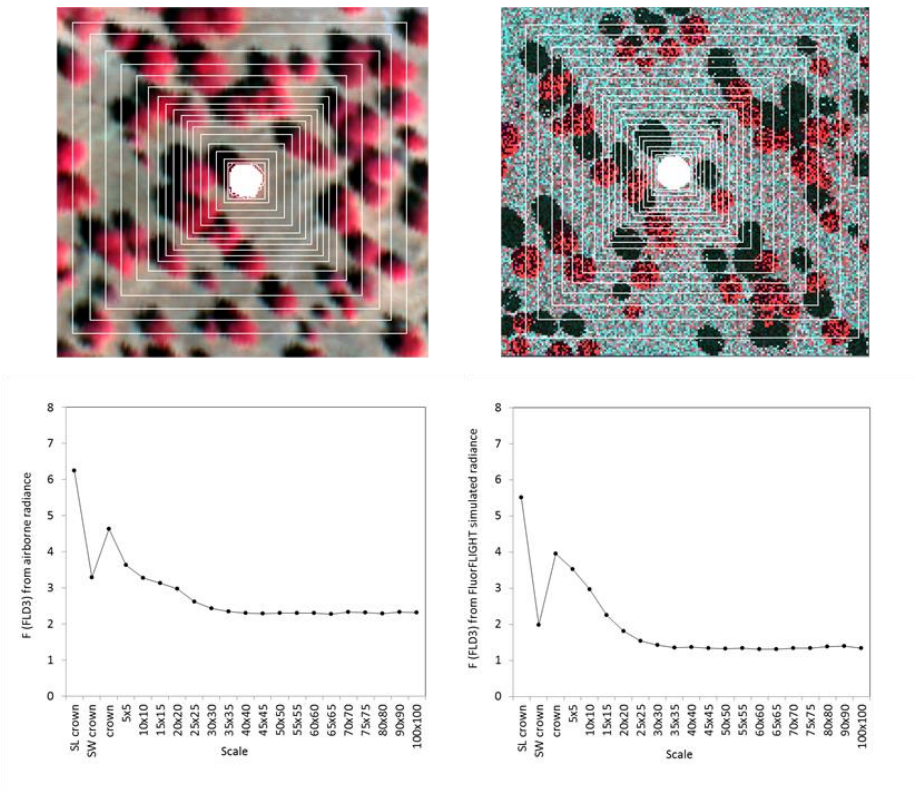

Fig. 4. Subplots emulating the aggregation effects due to the spatial resolution overlaid onto the micro-hyperspectral imagery acquired at 60 cm resolution (a) and a FluorFLIGHT simulated image (b), both in colour-infrared. F (FLD3) variation based on the hyperspectral image (c) and the simulated image (d) estimated from: sunlit pixels of the crown (SL crown), shadowed pixels of the crown (SW crown), full crown pixels (crown=SL+SW) and eighteen aggregated pixels from a 5x5 m window to a 100x100 m window.

FluorFLIGHT simulations were calculated for a set of leaf fluorescence quantum efficiency (F_i) values and forest structure scenarios. Leaf fluorescence signal was simulated with a varied range of F_i between 0 and 0.1. To cover the full range of canopy structural scenarios, a varied range of LAI (0-4), FC (0-100%) and density (10-200 trees/ha) were used to simulate the spectral response at the crown level (Fig. 5a) and at the aggregated canopy level (Fig. 5b).

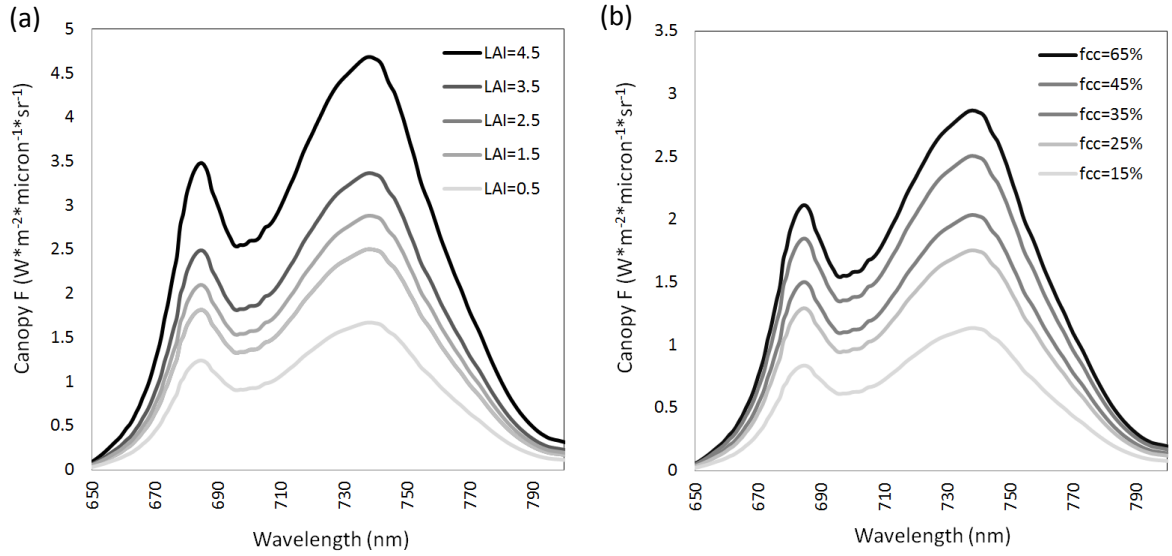

Fig. 5. Simulated canopy radiance including the effects of fluorescence using the FluorFLIGHT model for a varied range of leaf area index (LAI) (0.5-4.5) (a) and fractional cover (FC) (15-65%) (b). Fluorescence quantum yield efficiency at photosystem level (F_i=0.06). All other input parameters of the model were set using nominal values included in Table 1.

ii) Fluorescence retrieval with FluorFLIGHT and hyperspectral data for detecting forest stress.

The potential of using FluorFLIGHT to predict SIF from spatially aggregated pixels in a heterogeneous oak forest was analyzed. For this purpose, FluorFLIGHT was used in a multi-step LUT-based inversion scheme (Fig. 6) to retrieve full crown SIF from a complex scene accounting for the influence of scene structure and composition. The estimation of vegetation fluorescence emissions was assessed from a spatial aggregation of 30x30 m, which included variations in crown coverage and shadows and sunlit proportions. The lack of complex RTMs

to simulate SIF in heterogeneous canopies (Zarco-Tejada et al., 2013b) has constrained the progress on the fluorescence interpretation in forest canopies. As shown in Fig. 6, SIF was quantified by inversion based on the FLD3 estimated from the airborne image using the LUT derived from FluorFLIGHT. As a prior step, an optimal parameter combination of N, LAI, C_{a+b}, and FC was iteratively retrieved. Lastly, SIF retrievals were then validated based on ground measurements of the physiological variables related with the photosynthetic activity of the vegetation such as DEPS, ψ, and Fs.

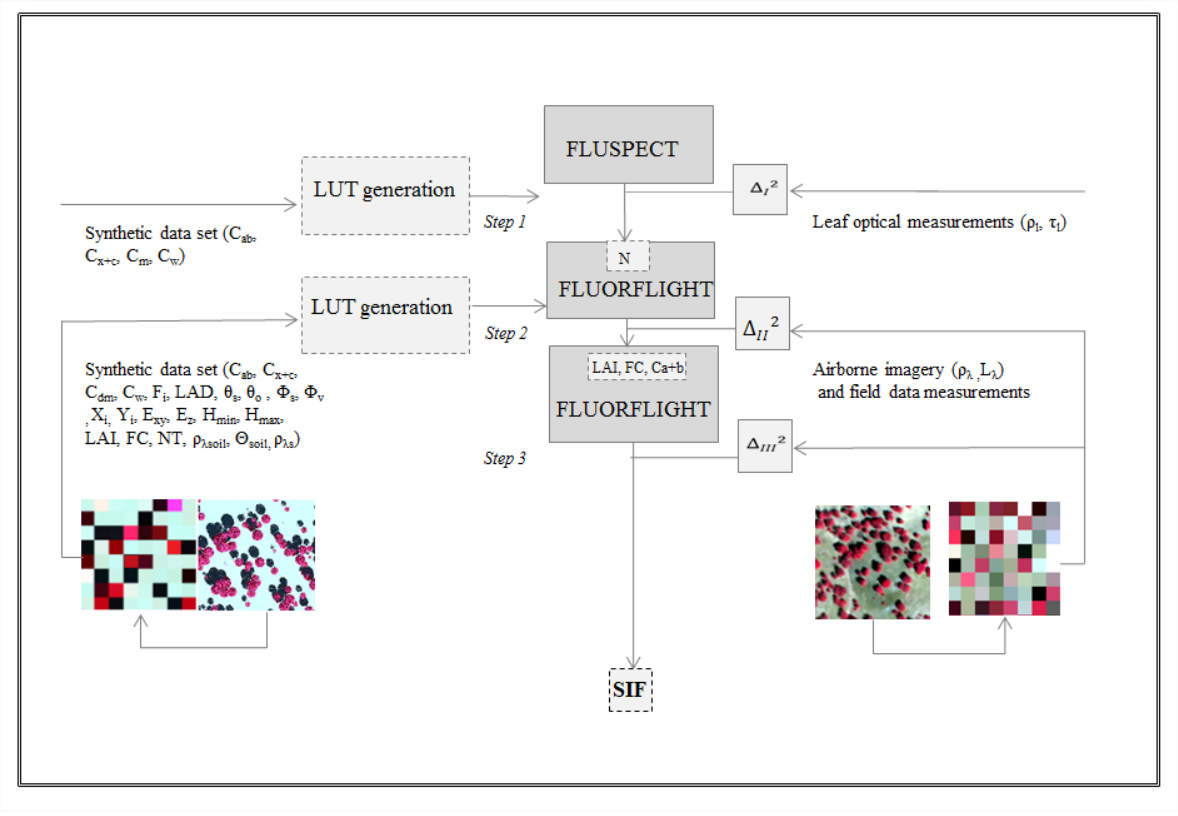

Fig. 6. Overview of the processing steps followed in the retrieval of sun-induced fluorescence (SIF) showing the input variables used for the simulations. Inputs description included in Table 1.

The detailed description of the inversion process shown in Fig. 6 is detailed below.

Step 1. N determination by minimizing the merit function (Δ_I):

$$\Delta_I{}^2 = \sum_n [(\rho_m(\lambda_i) - \rho^*(\lambda_i,\mathrm{N}))^2 + (\tau_m(\lambda_i) - \tau^*(\lambda_i,\mathrm{N}))^2] \quad (6)$$

Where $\rho_m(\lambda_i), \tau_m(\lambda_i)$ are the leaf reflectance and transmittance at wavelength λ measured from the field, and $\rho^*$and τ^* denote the modelled ones. A synthetic spectra database was simulated with FLUSPECT producing 1000 simulations with a set of *N* random values (1-4). Input parameters were set up to simulate the typical range of variation observed in the field Table 2.

Step 2. Green FC determination by minimizing the merit function (Δ_{II}):

For this purpose, FluorFLIGHT was used for retrieving an optimal set of vegetation parameters (FC, LAI and C_{a+b}) using a LUT-based inversion scheme using aggregated pixels of 30x30 m.

$$\Delta_{II}{}^2 = \sum_n [vi_m - vi^*(\Theta)]^2 \quad (7)$$

Where vi_m is the vegetation index used for the retrieval of each parameter calculated from measured canopy reflectance and $vi^*(\Theta)$ and from modelled canopy reflectance for a given set of input parameters Θ. FC and LAI were retrieved using the NDVI (Rouse et al., 1974); mean values of the range of possible solutions within the LUT were used since there is ambiguity between FC and LAI corresponding to a given VI value without additional constraints on allowable structure. C_{a+b} was retrieved using the RE (Zarco-Tejada et al., 2001) that showed robustness to shadow and structural effects in forest canopies. A synthetic spectra database was simulated with FluorFLIGHT producing 1000 simulations. Leaf input

parameters were set up to simulate the typical range of variation observed in the field (C_{a+b}=10-80 μg/cm^2; C_{x+c}=2-18 μg/cm^2; C_w=0.02; C_{dm}=0.01). Leaf level spectra were simulated using N=2.1 as derived from inversions of leaf-level optical measurements of field samples estimated above (Step 1). Leaf fluorescence signal was simulated with a varied range of F_i ranging between 0 and 0.1. The nominal inputs used at the leaf level are shown in Table 2.

At the canopy level, forest structure attributes such as tree height, crown diameter and LAI were randomly varied for different oak-forest cover structures to generate a range of FC between (0-100%). Table 2 shows the input parameters required by the model and the nominal variation range for the parameters used for canopy modelling with FluorFLIGHT. The spectral sampling of the simulations was initially adjusted to 1 nm covering a range for 400 to 1050 nm. Then, simulated images were resampled to the spectral bandwidth of the hyperspectral airborne sensor through Gaussian convolution. The inverted values of FC, LAI and C_{a+b} were obtained by matching measured and modelled LUT vi through (7) and finding the optimal parameter combination (Leonenko et al., 2013; Prieto-Blanco et al., 2009) and validated against FC, LAI and C_{a+b} field measurements.

Step 3. Fluorescence inversion using the inverted FC, LAI and C_{a+b} as multi-constraint regularization.

The simulated spectra with FluorFLIGHT were used here to retrieve SIF using the inverted values of FC, LAI and C_{a+b} (Step 2) as constraints in a regularization strategy attending to reduce the influence of structural canopy variables of the fluorescence signal.

$$\Delta_{III}{}^2 = \sum_n [F_m(FLD3) - F^*(FLD3,\Theta)]^2 \quad (8)$$

Where $F_m(FLD3)$, is the FLD3 calculated from measured canopy radiance and $F^*(FLD3,\Theta)$ is the FLD3 calculated from modelled canopy reflectance for a given set of input parameters Θ. In both cases, radiance spectra were extracted from 30x30 m aggregated pixels (Fig. 6). The inverted values of crown FLD3 and leaf F_i were obtained by matching measured and modelled LUT spectra through (8) and finding the optimal values.

Finally, model-based retrievals derived from hyperspectral imagery were compared to ground-truth fluorescence data. Additionally, results were also compared to other physiological variables collected on the ground.

3. Results.

3.1. Relationships between physiological variables and airborne F (FLD3).

The capability of F (FLD) of discriminating different functional status of the vegetation was analysed and compared to other vegetation spectral indices (Table 3). The relationships between F (FLD3) quantified from full crown vegetation pixels and different physiological variables (F_s, DEPS, and ψ) were statistically significant ($p < 0.01$) and stronger than the relationship with other physiological vegetation indices such as PRI or RE. The weakness relationship found was between the physiological variables and the NDVI, a sensitive indicator of canopy structure.

The high spatial resolution obtained by the hyperspectral imagery (60 cm resolution) enabled the identification of each scene components (Fig. 2), enabling the estimation of F (FLD3) from sunlit crowns pixels. The sunlit-crown F (FLD3) extracted was compared against (DEPS, ψ and F_s) measured at the tree-level, yielding (r^2= 0.63; p<0.001) (Fig. 7a) between

sunlit-crown F (FLD3) and ground measured DEPS. Slightly lower relationships were found by comparing F (FLD3) and ψ (r^2= 0.57; p<0.01) (Fig. 7b). Statistically significant relationships between sunlit-crown F (FLD3) and DEPS and ψ were consistent with the relationships obtained between leaf F_s and airborne F (FLD3) (r^2= 0.74; p<0.001) (Fig. 7c). These results indicate that SIF retrieved from sunlit vegetation radiance of the crowns was a good indicator of physiological status of the trees within the context of this study.

Table 3.

Correlation coefficient R between steady-state fluorescence yield (F_s), de-epoxidation state of the xanthophyll cycle (DEPS) and water potential (ψ) and crown-based spectral vegetation indices, including structural and physiological vegetation indices.

Functional-related indices		Fs		DEPS		ψ	
		R	*R2*	*R*	*R2*	*R*	*R2*
Fluorescence	FLD3	0.79	0.62***	-0.67	0.44**	0.71	0.5**
Photochemical reflectance index	PRI	-0.45	0.2	0.65	0.42**	-0.51	0.27*
Chlorophyll -RE	R750/R710	-0.24	0.06	0.13	0.02	-0.22	0.04
Structure-NDVI	NDVI	-0.16	0.02	0.16	0.03	-0.18	0.03

Non-significant	P>0.05
*Significant***	P<0.01
*Highly significant***	P<0.001

It was also observed that healthy trees (FPC1) showed higher F_s and ψ and lower DEPS while affected trees (FPC3) showed the opposite, with moderate level of affectation (FPC2) in between. These results showed that sunlit-crown F (FLD3) was also sensitive to the stress levels, tracking the physiological change forced by forest decline processes.

Additionally, the F (FLD3) was calculated from spectra extracted from aggregated pixels from a 30x30 m window using as central point the location of each tree. The SIF signal retrieved from aggregated pixels was lower than that extracted from sunlit crown pixels with F (FLD3) values ranged between (1.9-4.9 and 2.5-8) $Wm^{-2}\mu m^{-1}sr^{-1}$ respectively (Fig. 7c, d). As it is shown in Fig. 7d, the sensitivity to F_s ground-data was lower with F (FLD3) retrieved from aggregated radiance pixels, yielding a (r^2= 0.25; statistically non-significant). These

results demonstrates the expected effect caused by the canopy architecture on SIF retrieved from mixed pixels, and therefore, the need of modelling those effects while using coarse-spatial resolution images.

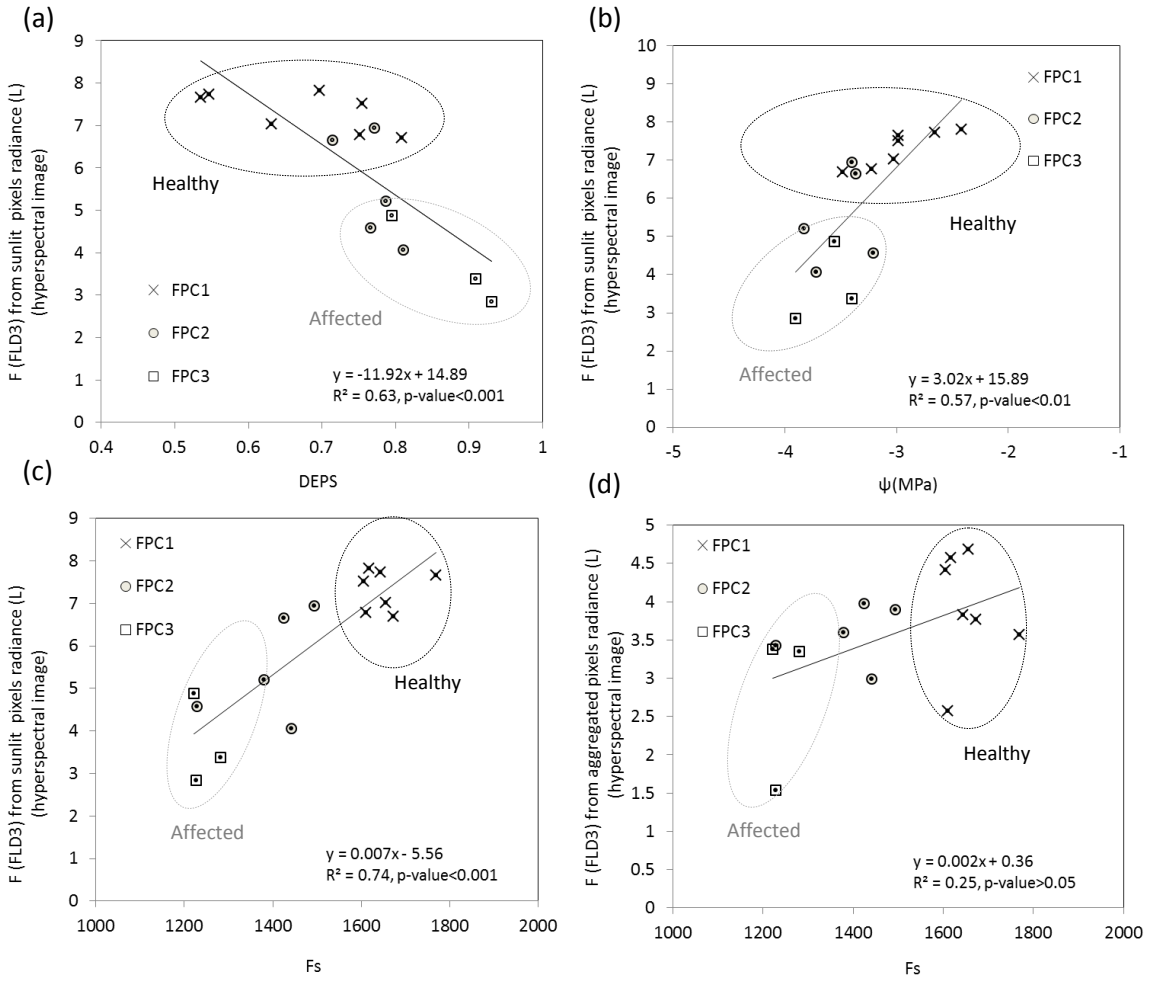

Fig. 7. Relationship between de-epoxidation state of the xanthophyll cycle (DEPS) (a) and water potential (b) against F (FLD3) from sunlit pixel radiance L retrieved from the hyperspectral image. Relationships between steady-state fluorescence yield (F_s) ground-data measurements of 15 oak trees and airborne-based F (FLD3) retrieved from sunlit pixel radiance (c) and 30x30 m aggregated pixels radiance (L) retrieved from the hyperspectral image (d). Trees with higher and lower level of affectation are highlighted within a dashed grey and black line respectively.

3.2. Modelling forest structural effects on SIF at the canopy level.

The sensitivity of the fluorescence signal to the variation in canopy structural components based on the relationships between crown SIF and SIF from 30x30 m aggregated pixels is presented in Fig. 8. F (FLD3) was retrieved for a range of LAI, tree density and percentage of FC values showing the influence of scene components on fluorescence signal from full crowns (Fig. 8a) and aggregated pixels (Fig. 8b).

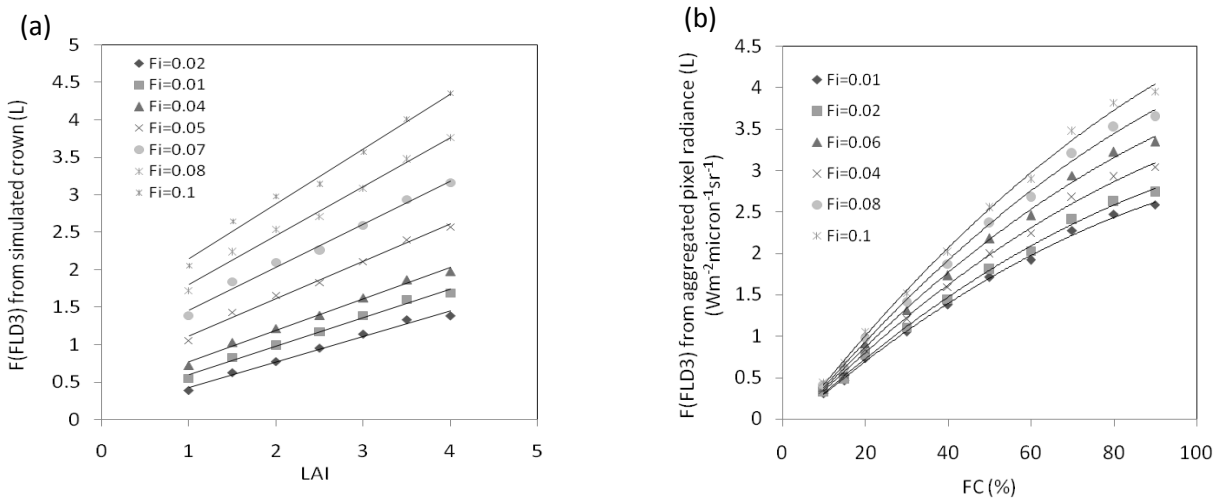

Fig. 8. Effects of forest structural variables on simulated canopy fluorescence (FLD3) as a function of LAI (0-5) at the crown level (a) and fractional cover FC (10-90%) at the canopy level (b). All other input parameters of the model were set using nominal values included in Table 1.

The sensitivity of SIF to variations in forest canopy structure is higher at lower values of LAI and FC, especially with aggregated pixels (Fig. 8b). According to these results, SIF signal variations at the crown and canopy level can only be directly linked to variations in photosynthetic activity when structural parameters remain constant (Fig. 8). Only in this case, F (FLD3) increased as the F_i input parameters increased.

Additionally, FluorFLIGHT simulations were used to develop relationships between sunlit crown pixels, crown pixels and aggregated pixels as a function of FC and LAI. As shown in Fig. 9, LAI and FC were varied to generate a range between 1-4 and 10-100%, respectively.

(a) (b)

554

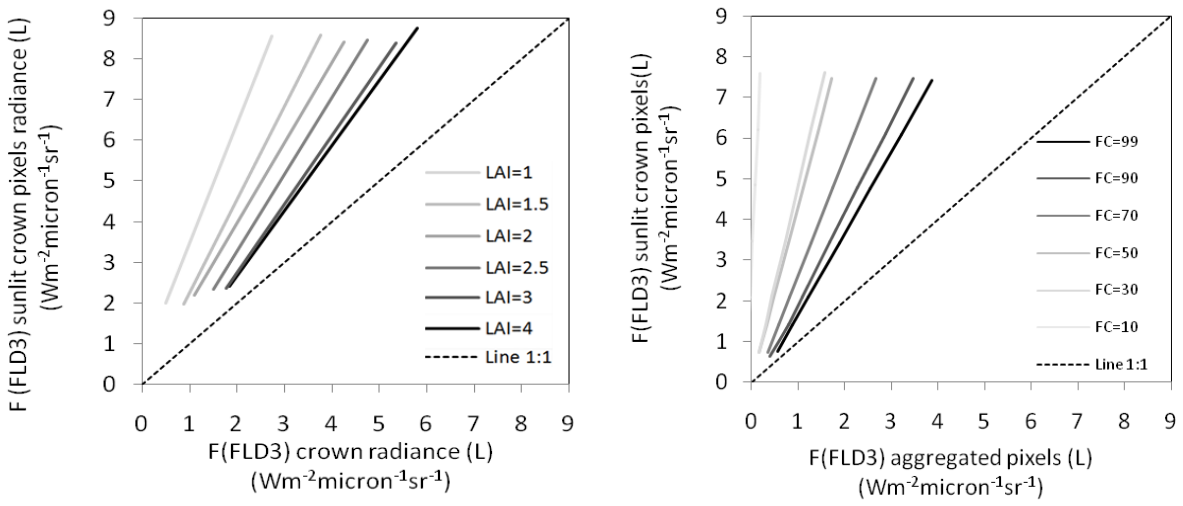

555 **Fig. 9.** Relationships between FluorFLIGHT simulations of canopy L obtained from sunlit crown
556 pixels and full crowns as a function of LAI (1-4) (a). Relationships between FluorFLIGHT
557 simulations of crown L obtained from sunlit crowns and aggregated pixels as a function of FC (10-
558 90%) (b).

559

560 The simulated SIF was calculated using the FLD method for the spectral radiance extracted
561 from sunlit crowns and then compared to different components of the scene such as full
562 crown (Fig. 9a) and aggregated pixels of the scene (Fig. 9b). Modelling results show that the
563 SIF signal retrieved from exposed crown and full crown pixels is higher than for aggregated
564 pixels. The differences are even significant between the SIF signal retrieved from sunlit
565 pixels and full crown pixels (Fig. 9a) with slightly higher values for exposed crowns. The
566 results of quantifying SIF from 30x30 m aggregated pixels as a function of LAI (Fig.9a) and
567 FC (Fig. 9b) show the large effects of both parameters of the fluorescence quantification. The
568 contribution of a small percentage of sparse grass component on the soil reflectance
569 measured from ground measurements hindered F (FLD3) to reach values slightly above zero.

570 Additionally, (Fig. 10) shows the impact on SIF retrieval through the FLD3 method when it
571 is retrieved from different levels of aggregation (sunlit crown pixels, full crown pixels and
572 aggregated pixels) for a varied range of F_i, LAI and FC. Comparing the results obtained for

573 the different levels of aggregation, changes in aggregated pixels caused highest uncertainties
574 in retrieved F (FLD3), followed by full crown pixels and shaded pixels. In contrast, LAI
575 variations exerted a small variation in F (FLD3) retrieved from sunlit pixels. The SIF signal
576 retrieved from sunlit crowns ranged between 0 and 8 $Wm^{-2}\mu m\text{-}1sr^{-1}$, decreasing the maximum
577 range with the level of aggregation to 5.2, 3.6 and 1 $Wm^{-2}\mu m^{-1}sr^{-1}$ for full crown, aggregated
578 pixels and shaded crowns, respectively. Moreover, the SIF signal retrieved from aggregated
579 pixels was less sensitive to F_i variation than the SIF signal retrieved from sunlit pixels. SIF
580 signal in shaded crown pixels had minimal sensitivity to F_i variations.

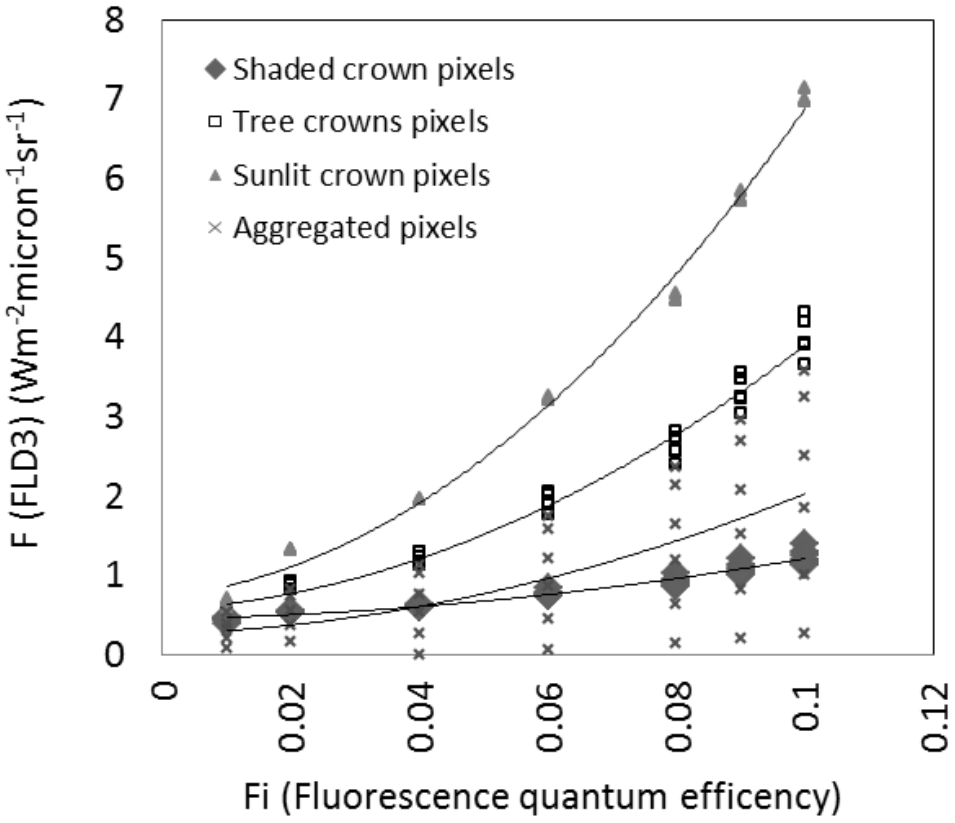

581

582 **Fig. 10.** Comparison of FluorFLIGHT model-based fluorescence quantum efficiency (F_i) and F
583 (FLD3) retrieved from shaded and sunlit crown pixels, full crown pixels and aggregated pixels as a
584 function of LAI (0-4) and FC (0-100%).

585

586 FluorFLIGHT model simulations obtained using a random synthetic data set of values within
587 the typical range of variation observed in the field (Table 2) are shown in Fig. 11. F (FLD3)

calculated from aggregated radiance pixels was weakly related to F_i due to the large variability in FC percentages and LAI within simulations (Fig. 11a). A cross-comparison of simulation results generated from different levels of aggregation shows that the retrieval of fluorescence improved using fluorescence radiance data from full crown pixels (r^2=0.75; p<0.001) and improving even more when sunlit crown pixels were used to calculate SIF (r^2=0.91; p<0.001) (Fig. 11b, c). This result was caused by the increase of the effects of vegetation structure and percentages of soil and shadows in aggregated pixels. The SIF signal retrieved from sunlit crown pixels is less affected by such effects, increasing its sensitivity to leaf fluorescence quantum efficiency.

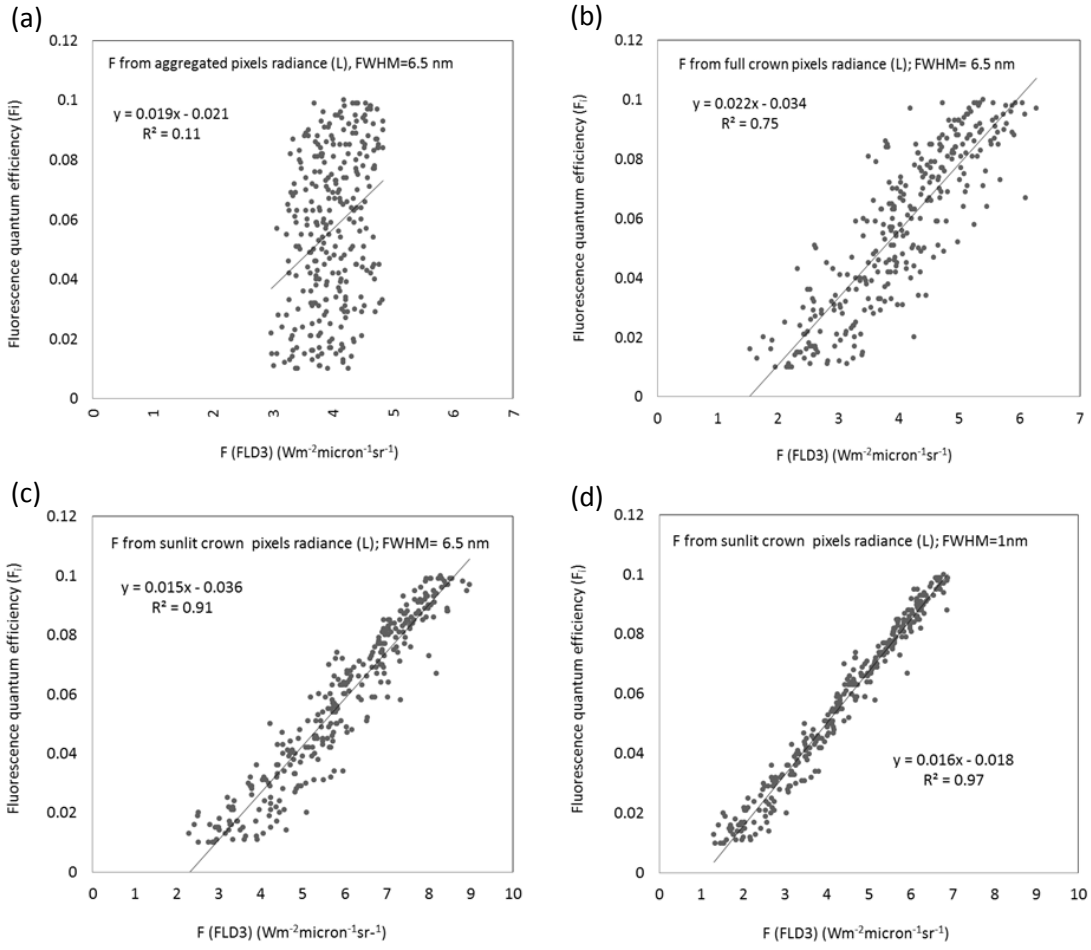

Fig 11. Relationships between the simulated FluorFLIGHT fluorescence quantum efficiency retrieved (FLD3 method) from synthetic spectra retrieved from 30x30 m aggregated pixels (a), full crown pixels (b) and sunlit crown pixels at 6.5 nm (c) and at 1 nm (d). LAI (0-4) and FC (40-60%). All other input parameters of the model were set using nominal values included in Table 1.

602 The sensitivity of SIF signal retrieved from sunlit crowns was further analysed to determine
603 the impact of using FWHM spectral resolution lower than 1 nm. FluorFLIGHT simulations in
604 Fig. 11c, d show the results of estimating SIF signal with FLD3 in-filling method against the
605 fluorescence simulated at 1 nm resolution and 6.5 nm resolution (as a proxy of the spectral
606 resolution of the micro-hyperspectral imager used in this study). SIF signal retrieved at 6.5
607 nm and 1 nm had relatively similar accuracies, yielding r^2=0.90 (for 6.5 nm data) and r^2=0.97
608 (for 1 nm data).

609 Therefore, the forest structure and composition were shown to play the major role in retrieved
610 SIF due to the confounding effects caused on aggregated pixels, with much less effect caused
611 by the spectral bandwidth.

612

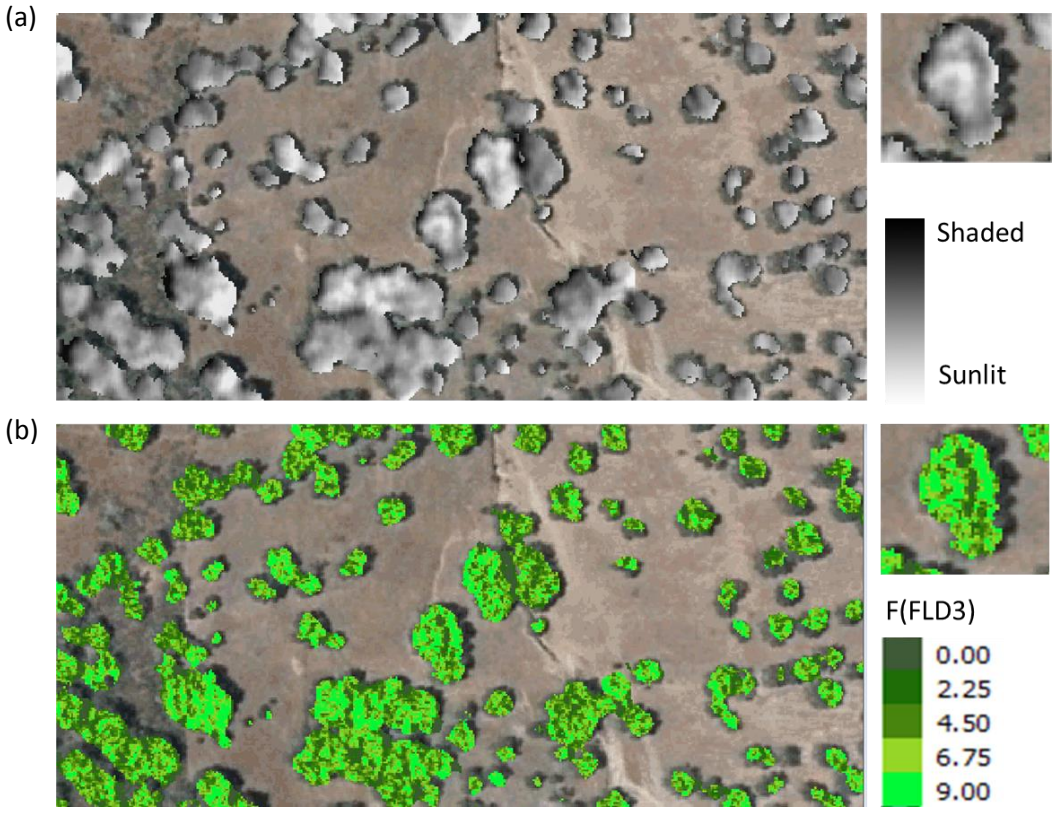

613

614 **Fig. 12**. (a) Sunlit and shadowed component identification of the crown on the micro-hyperspectral
615 imagery. (b) SIF map showing different values between sunlit and shaded crown F (FLD3).

These modelling results demonstrate the difficulties of interpreting SIF from coarse resolution images where each aggregated pixel includes a large variety of percentages of sunlit and shaded vegetation and soil. The effect of the illumination condition of the crowns corroborates the need to separate the two crown factions as is shown with high resolution SIF maps (Fig 12).

Accounting for variations in those percentages, FluorFLIGHT was then used to retrieve SIF from 30x30m aggregated pixels. The estimation of leaf F_i and crown F (FLD3) through FluorFLIGHT model inversion is shown in (Fig. 13).

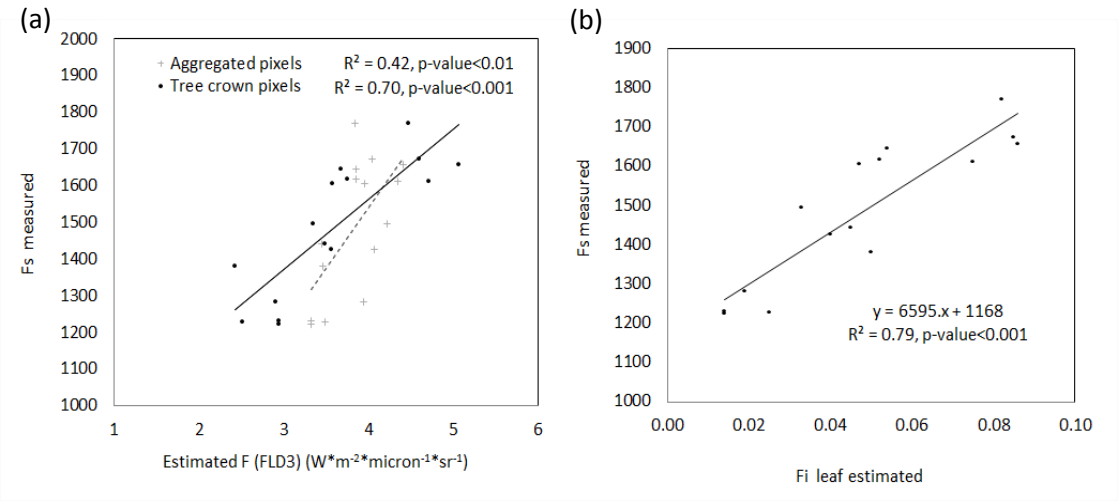

Fig. 13. Relationships between F_s ground-data measurements and fluorescence estimations retrievals using FluorFLIGHT applied to aggregated pixels without accounting for pixel aggregation (30x30 m aggregated pixels) and accounting for pixel aggregation (full crown pixels) with FluorFLIGHT (a) Leaf level relationship between F_s ground-data measurements and fluorescence quantum yield estimated with FluorFLIGHT (b).

Fig 13a shows the relationship between F_s ground-data and the SIF signal retrieved by inversion using FluorFLIGHT through the FLD3 method from aggregated pixels (30x30 m). According to these results, pixel aggregation affected the accuracy in SIF retrieval (r^2=0.42) when pixel aggregation was not considered. The retrieval accuracy was significantly improved when accounting for the effects of scene components and FC (r^2=0.70). When the F_i was retrieved from FluorFLIGHT accounting for the percentage cover within each pixel,

637 the relationship with F_s ground-data measurements were significantly related (r^2=0.79, Fig.
638 13b). These results are consistent with the relationship found between F_i and the airborne-
639 based F (FLD3) retrieved from aggregated pixels and sunlit pixels (Fig 11a, c). Fig.14 shows
640 the output maps after the inversion approach applied at the crown level. The map shows the
641 spatial variability of fluorescence estimates within the oak forest based on the F (FLD3) and
642 the F_i inverted from FluorFLIGHT (Fig. 14). The spatial distribution of fluorescence agrees
643 with the spatial pattern of *Phytophthora* infections showing different susceptibility levels
644 from trees nearby.

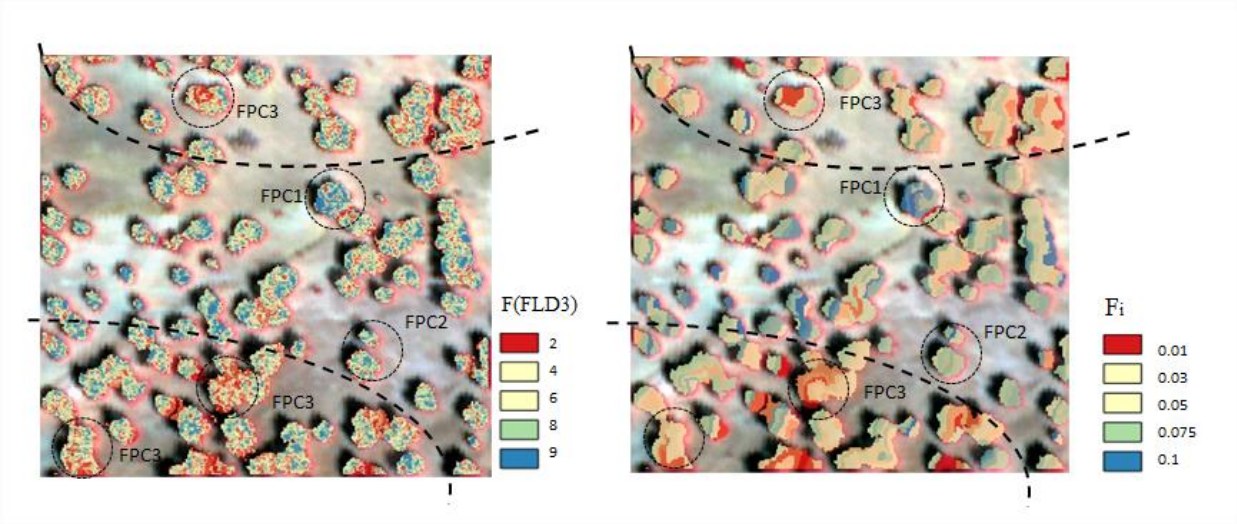

645

646 **Fig. 14.** F_i retrieval at the crown level estimated from the 60-cm hyperspectral image using the
647 fluorescence in-filling method F (FLD3) within the oak forest.

648

649 **4. Discussion.**

650 The consistent relationship between the fluorescence signal SIF retrieved from imagery and
651 physiological variables (see Fig. 7) supports the hypothesis that SIF signal is a good indicator
652 of the physiological status of the trees. Although similar observations have been made within
653 other species e.g., for coastal shrubs (Naumann et al., 2008); for vineyards and orange trees
654 (Zarco-Tejada et al., 2013a and Zarco-Tejada et al., 2016), this is the first attempt showing a

655 consistent relationship between SIF calculated using the FLD3 method from image pixels and
656 physiological variables such as DEPS, F_s or Ψ across different functional forest health
657 conditions (FPC 1, 2 and 3). In this particular case, SIF was demonstrated to be a good
658 indicator of the susceptibility of oak species to damage associated with root pathogen on
659 water relations. Other physiological vegetation indices such as PRI should be also further
660 explored and potentially applied in combination with SIF. Stress-induced damage in oaks is
661 related with an increase in Ψ (absolute values), an increase in the deposition of xanthophylls
662 and a decline in the chlorophyll fluorescence emission (Fig. 7). These results are promising
663 because the early detection of the decline in the physiological condition of the trees is
664 essential to successfully control and manage threatened forests.

665 A major benefit of using a 60-cm hyperspectral image is that it enables identification of the
666 fluorescence signal emitted by the different components of the canopy. When comparing the
667 relationship between the ground-based F_s against the SIF extracted from sunlit crown and
668 30x30 m aggregated image pixels (r^2= 0.74 and r^2= 0.25, respectively), we observe a
669 significant decrease in the coefficient of determination when using coarse pixel radiance. The
670 slope of the SIF extracted from sunlit crowns is greater than for 30x30 m aggregated pixels,
671 showing therefore a greater rate of change, probably increased by the reduced effects of the
672 background in vegetation sunlit pixels. The sensitivity of remotely measured SIF to pixel
673 aggregations is mainly produced by the natural variations in canopy structure and chlorophyll
674 concentration of a heterogeneous canopy (Verrelst et al., 2016; Zarco-Tejada et al., 2013b).
675 The variation in SIF showed changes as a function of the pixel aggregation level with the
676 highest value yielded with aggregated pixels from the sunlit part of the crown. SIF retrieved
677 from aggregated resolutions with a higher percentage of shadows (SW crown) and soil
678 yielded lower values. Beyond a spatial resolution of 25x25 m, where the number of soil
679 pixels is twice as large as the crown, the aggregation level no longer exerted any influence on

F (FLD3). F (FLD3) derived from simulated data and from the hyperspectral image show similar effects: the highest F (FLD3) values corresponded to sunlit crown pixels, and were approximately 25% higher than F (FLD3) extracted from full crown pixels (simulated images) and 32% higher (hyperspectral images). Shaded crowns dramatically reduced the simulated fluorescence, being 66% lower than F (FLD3) values from sunlit crowns. Shaded crowns had a large effect on the radiance signal derived from hyperspectral images by reducing up to 47% the F (FLD3) values as compared to the sunlit part of the crown. Both, FluorFLIGHT-based F (FLD3) and hyperspectral image-based F (FLD3) were significantly reduced with the increase in pixel aggregation level. These results demonstrate the difficulty of quantifying the fluorescence signal using aggregated pixels beyond the crown scale in heterogeneous canopies.

Zarco-Tejada et al., (2013b) investigated the possibility of estimating full crown fluorescence from aggregated pixels. Such efforts addressed the effect of canopy structure of the SIF signal, raising important questions about the need to develop new models to simulate SIF from heterogeneous canopies. The main limitation of their study was the use of the coupled FluorMODleaf + FluorSAIL accounting for the geometry through FLIM, which did not take into account scene components such as crown overlapping or illumination conditions within the canopy in the simulations. The FluorFLIGHT model used in this study is a 3-D RTM that allowed the study of the effects caused by the canopy structure, including sunlit and shaded proportions of the crowns and background effects on the retrieval of fluorescence signal from mixed pixels. The experimental and modelling results demonstrated that the estimation of SIF from sunlit crown pixel radiance is a critical issue affecting the estimation accuracy as the mixture with shaded and background pixels increases.

In order to provide a proper interpretation of SIF signal retrieved at global scales it is crucial to decouple the fluorescence signal produced by the photosynthetic activity and the

confounding effects produced by the canopy structure and multiple scattering (Damm et al., 2014; Verrelst et al., 2015). The FluorFLIGHT simulation analysis presented here suggests that the canopy structure and composition may affect significantly the quantification of SIF from coarse resolutions at global scale. These results confirm some recent efforts done by other authors in order to provide insights into the key variables that drive SIF from vegetation canopies using RTM approaches within the SCOPE model (Verrelst et al., 2016). However, multiple scattering effects within the canopy cannot be addressed with the 1-D RTM SCOPE. Additionally, FluorFLIGHT used here also investigated the effect of scene components such as the percentage of vegetation or the illumination condition on the interpretation of fluorescence signal retrieved from forest heterogeneous canopies. The proportion of sunlit green vegetation absorbs more light and hence produce a higher SIF intensity (Genty et al., 1989) which explains the higher values in SIF retrieval on sunlit crowns using the FLD3 method. These results were demonstrated here through both the model simulation approach and experimental data.

Another important issue that requires attention is the potential effect of the spectral resolution on the retrieval of fluorescence, which has been questioned by some authors (Damm et al., 2014). To raising awareness on this issue, the spectral resolution of the hyperspectral sensor used in this study (6.5 nm) was also analysed. Both, experimental and simulation analysis demonstrated that the retrieval of fluorescence is feasible with such spectral resolution. SIF accuracy retrievals are only slightly diminished by using a spectral resolution of 6.5 nm compared with the effect produced by other factors such as forest structure and density. The expected deviation between absolute SIF values retrieved at 1 nm and with 6.5 nm FWHM (with high sampling intervals) do not likely affect the conclusions obtained in studies such as this one, which focuses in fluorescence retrievals for stress detection purposes rather than the absolute quantification of SIF values. In these studies, the variation of fluorescence in relative

terms enables the assessment of early stress related to disease severity levels and forest decline variability.

Besides the intrinsic factors that modulate the SIF at the canopy level, the pixel aggregation used affects the estimated intensity. In particular, the accuracy of SIF retrieved from aggregated pixels beyond the crown level is uncertain because the pixel mixture may include the confounding effects of shaded pixels and background soil, decreasing the absorption in the O_2-B band, and therefore, the overall magnitude of the F-signal. A more refined 3-D canopy model including physiological, aerodynamic and geometry variables would be needed to better analyse the physiological regulation of the fluorescence yield as a function of micrometeorological drivers. Nevertheless, the results of the present study showed a strong improvement in the retrieval of SIF at the leaf level from coarse resolution pixels based on the inversion of FluorFLIGHT accounting for structural variables (r^2=0.70) compared to the results obtained ignoring those effects (r^2=0.42).

Therefore, these results suggest that the use of a 3-D RTM, such as FluorFLIGHT, may improve the estimation of SIF at global scales. SIF estimation at the crown level becomes particularly critical with invasive plant pathogens affecting individual trees alternately and selectively within the forest canopy. This is the case of sudden oak death disease progression at local and spatial scales (Ramage et al., 2012). Local patchiness in disease presence/severity can be clearly observed with the high local variability of the F_i inversion map estimated at the oak site. Hence, mapping fluorescence emission based on FluorFLIGHT model inversion approaches sets a new standard in the early detection of stress effects towards precision forestry. The early detection of hotspot locations (focus of infection or decline) might help to combat forest decline processes, and in case of *Phytophthora* infections, prevent the spread of the infection.

These results are of particular interest for the FLEX mission, approved as ESA's Earth Explorer 8 (Drusch et al., 2016), which will with provide fluorescence emission at finer spatial scale than currently possible, and potential to resolve full fluorescence emission spectrum with further information on stress attribution (Ač et al., 2015; Cogliati et al., 2015). There are still many challenges for measurement of SIF from space; further validation studies need to be undertaken to assess modelling results and the effect of environmental stress factors on ecophysiological traits and forest productivity. Another important issue that requires attention is the potential application of these methods to different forest types increasingly complex in terms of structure and tree species composition. The canopy structure and spatial heterogeneity of the open-and-sparse oak woodland studied here may have a different effect on global SIF estimates to other types of land covers: with higher canopy density (closed forest canopies), with higher heterogeneity in species and/or soil composition or higher vertical heterogeneity within forest canopies.

It is important to highlight the difficulties of validating the estimation of SIF from spaceborne sensors over forest canopies, which encompass challenging experimental field campaigns and sampling conditions. The use of very high resolution airborne hyperspectral imagery as used in this and similar studies may be valuable. More studies supporting the validation of SIF are foreseen to improve our understanding in the link between SIF and photosynthetic activity with a greater degree of confidence. SIF retrievals using FluorFLIGHT should be further validated for different types of canopies and physiological conditions for monitoring forest decline processes.

5. Conclusions.

Measuring SIF remotely is potentially a valuable tool to track the health and productivity of forest but also brings important challenges. This study gives the first 3-D model of canopy fluorescence, combined with an original field campaign aimed at quantifying the link between canopy physiology and detection at scales suitable for satellite remote sensing. The results show a link between physiologically based indicators and SIF retrieval from hyperspectral remote sensing for an oak forest affected by root pathogen infections and water stress.

Model estimations against in-situ measurements conducted over the oak forest demonstrated significant utility of SIF for precision physiological condition characterization. The FluorFLIGHT model enabled the estimation of sunlit vegetation fluorescence from coarse pixels (r^2=0.79, p<0.01) accounting for the large effects produced by the FC and canopy structure. The model inversion approach at three steps, which progressively approximates the observed canopy structure heterogeneity from the study sites, showed improvements in the estimation of leaf-based fluorescence measurement.

The results presented in this study demonstrated the fluorescence signal retrieved from mixed pixels is significantly affected by the effects caused by the illumination condition and the structural component of the canopy (r^2=0.42). Those effects are intrinsic to all radiance spectral retrieved from aggregated pixels irrespective of the sample size, but get increasingly critical with increasing levels of aggregation (pixel size). In particular, the SIF signal was significantly lower when retrieved from coarse pixels (lower than 10x10 m resolution) than from sunlit pixel crowns (<50%). Fluorescence retrieval using FluorFLIGHT and accounting for pixel aggregation minimized the impact of the canopy structure and other scene components improving the accuracy of the estimations (r^2=0.70).

Acknowledgements

This study was conducted under the Marie Curie Intra-European Fellowship for Career Development. Data collection was partially supported by the THERMOLIDAR FP7 Project and the QUERCUSAT project from the Spanish funding agency "Ministerio de Economia y Competitividad". The authors are most grateful to the Treesat research group (ERSAF, University of Cordoba, Spain) for the support provided during the field campaigns.

References

Ač, A., Malenovský, Z., Olejníčková, J., Gallé, A., Rascher, U., Mohammed, G., 2015. Meta-analysis assessing potential of steady-state chlorophyll fluorescence for remote sensing detection of plant water, temperature and nitrogen stress. Remote Sens. Environ. 168, 420–436. doi:10.1016/j.rse.2015.07.022

Bye, I.J., North, P.R.J., Los, S.O., Kljun, N., Rosette, J.A.B., Hopkinson, C., Chasmer, L., Mahoney, C., 2017. Estimating forest canopy parameters from satellite waveform LiDAR by inversion of the FLIGHT three-dimensional radiative transfer model. Remote Sens. Environ. 188, 177-189. doi: 10.1016/j.rse.2016.10.048

Cogliati, S., Verhoef, W., Kraft, S., Sabater, N., Alonso, L., Vicent, J., Moreno, J., Drusch, M., Colombo, R., 2015. Retrieval of sun-induced fluorescence using advanced spectral fitting methods. Remote Sens. Environ. 169, 344–357. doi:10.1016/j.rse.2015.08.022

Damm, A., Guanter, L., Laurent, V.C.E., Schaepman, M.E., Schickling, A., Rascher, U., 2014. FLD-based retrieval of sun-induced chlorophyll fluorescence from medium spectral resolution airborne spectroscopy data. Remote Sens. Environ. 147, 256–266. doi:10.1016/j.rse.2014.03.009

824 Damm, A., Guanter, L., Verhoef, W., Schläpfer, D., Garbari, S., Schaepman, M.E., 2015.
825 Impact of varying irradiance on vegetation indices and chlorophyll fluorescence
826 derived from spectroscopy data. Remote Sens. Environ. 156, 202–215.
827 doi:10.1016/j.rse.2014.09.031

828 Drusch, M., Moreno, J., Del Bello, U., Franco, R., Goulas, Y., Huth, A., Kraft, S., Middleton,
829 E. M., Miglietta, F., Mohammed, G., Nedbal, L., Rascher, U., Schüttemeyer, D.,
830 Verhoef, W., 2016. The FLuorescence EXplorer Mission Concept-ESA's Earth
831 Explorer 8. *IEEE Transactions on Geoscience and Remote Sensing* , vol. PP, (99), pp.1-
832 12. doi: 10.1109/TGRS.2016.2621820

833 Duffour, C., Olioso, A., Demarty, J., Van der Tol, C., Lagouarde, J.-P., 2015. An evaluation
834 of SCOPE: A tool to simulate the directional anisotropy of satellite-measured surface
835 temperatures. Remote Sens. Environ. 158, 362–375. doi:10.1016/j.rse.2014.10.019

836 Feret, J.-B., François, C., Asner, G.P., Gitelson, A.A., Martin, R.E., Bidel, L.P.R., Ustin,
837 S.L., le Maire, G., Jacquemoud, S., 2008. PROSPECT-4 and 5: Advances in the leaf
838 optical properties model separating photosynthetic pigments. Remote Sens. Environ.
839 112, 3030–3043. doi:10.1016/j.rse.2008.02.012

840 Ferraz, J., Casas, A.T., Caetano, P., 2000. El decaimiento y muerte de encinas en tres dehesas
841 de la provincia de Huelva. Bol. Sanid. Veg. Plagas 26, 447–464.

842 Franck, F., Juneau, P., Popovic, R., 2002. Resolution of the Photosystem I and Photosystem
843 II contributions to chlorophyll fluorescence of intact leaves at room temperature.
844 Biochim. Biophys. Acta BBA - Bioenerg. 1556, 239–246. doi:10.1016/S0005-
845 2728(02)00366-3

Frankenberg, C., Fisher, J.B., Worden, J., Badgley, G., Saatchi, S.S., Lee, J.-E., Toon, G.C., Butz, A., Jung, M., Kuze, A., Yokota, T., 2011. New global observations of the terrestrial carbon cycle from GOSAT: Patterns of plant fluorescence with gross primary productivity. Geophys. Res. Lett. 38, L17706. doi:10.1029/2011GL048738

Gamon, J.A., Peñuelas, J., Field, C.B., 1992. A narrow-waveband spectral index that tracks diurnal changes in photosynthetic efficiency. Remote Sensing of Environment 41, 35–44. doi:10.1016/0034-4257(92)90059-S

Genty, B., Briantais, J.-M., Baker, N.R., 1989. The relationship between the quantum yield of photosynthetic electron transport and quenching of chlorophyll fluorescence. Biochim. Biophys. Acta BBA - Gen. Subj. 990, 87–92. doi:10.1016/S0304-4165(89)80016-9

Guanter, L., Frankenberg, C., Dudhia, A., Lewis, P.E., Gómez-Dans, J., Kuze, A., Suto, H., Grainger, R.G., 2012. Retrieval and global assessment of terrestrial chlorophyll fluorescence from GOSAT space measurements. Remote Sens. Environ. 121, 236–251. doi:10.1016/j.rse.2012.02.006

Hernández-Clemente, R., Navarro-Cerrillo, R.M., Suarez, L., Morales, F., Zarco-Tejada, P.J., 2011. Assessing structural effects on PRI for stress detection in conifer forests. Remote Sens. Environ. 115, 2360–2375. doi:10.1016/j.rse.2011.04.036

Hernández-Clemente, R., Navarro-Cerrillo, R. M., Ramírez, F.J.R., Hornero, A., Zarco-Tejada, P.J. 2014. A Novel Methodology to Estimate Single-Tree Biophysical Parameters from 3-D Digital Imagery Compared to Aerial Laser Scanner Data. Remote Sensing, 6, 11, 11627–11648. doi: 10.3390/rs61111627

Jacquemoud, S., Baret, F., 1990. PROSPECT: A model of leaf optical properties spectra. Remote Sens. Environ. 34, 75–91. doi:10.1016/0034-4257(90)90100-Z

869 Joiner, J., Yoshida, Y., Vasilkov, A.P., Schaefer, K., Jung, M., Guanter, L., Zhang, Y.,
870 Garrity, S., Middleton, E.M., Huemmrich, K.F., Gu, L., Belelli Marchesini, L., 2014.
871 The seasonal cycle of satellite chlorophyll fluorescence observations and its
872 relationship to vegetation phenology and ecosystem atmosphere carbon exchange.
873 Remote Sens. Environ. 152, 375–391. doi:10.1016/j.rse.2014.06.022

874 Kraft, S., Bello, U.D., Bouvet, M., Drusch, M., Moreno, J., 2012. FLEX: ESA's Earth
875 Explorer 8 candidate mission, in: 2012 IEEE International Geoscience and Remote
876 Sensing Symposium. Presented at the 2012 IEEE International Geoscience and Remote
877 Sensing Symposium, pp. 7125–7128. doi:10.1109/IGARSS.2012.6352020

878 Krause, G.H., Weis, E., 1984. Chlorophyll fluorescence as a tool in plant physiology.
879 Photosynth. Res. 5, 139–157. doi:10.1007/BF00028527

880 Kuze, A., Suto, H., Nakajima, M., Hamazaki, T., 2009. Thermal and near infrared sensor for
881 carbon observation Fourier-transform spectrometer on the Greenhouse Gases
882 Observing Satellite for greenhouse gases monitoring. Appl. Opt. 48, 6716–6733.

883 Larbi, A., Abadía, A., Morales, F., Abadía, J., 2004. Fe Resupply to Fe-deficient Sugar Beet
884 Plants Leads to Rapid Changes in the Violaxanthin Cycle and other Photosynthetic
885 Characteristics without Significant de novo Chlorophyll Synthesis. Photosynth. Res.
886 79, 59–69. doi:10.1023/B:PRES.0000011919.35309.5e

887 Leonenko, G., Los, S.O., North, P.R.J., 2013. Statistical Distances and Their Applications to
888 Biophysical Parameter Estimation: Information Measures, M-Estimates, and Minimum
889 Contrast Methods. Remote Sens. 5, 1355–1388. doi:10.3390/rs5031355

890 Maurel, M., Robin, C., Capron, G., Desprez-Loustau, M.-L., 2001. Effects of root damage
891 associated with *Phytophthora cinnamomi* on water relations, biomass accumulation,

892 mineral nutrition and vulnerability to water deficit of five oak and chestnut species. For.
893 Pathol. 31, 353–369. doi:10.1046/j.1439-0329.2001.00258.x

894 Miller, J., 2005. Development of a Vegetation Fluorescence Canopy Model.

895 Moralejo, E., García-Muñoz, J.A., Descals, E., 2009. Susceptibility of Iberian trees to
896 *Phytophthora ramorum* and *P. cinnamomi.* Plant Pathol. 58, 271–283.
897 doi:10.1111/j.1365-3059.2008.01956.x

898 Natalini, F., Alejano, R., Vázquez-Piqué, J., Cañellas, I., Gea-Izquierdo, G., 2016. The role of
899 climate change in the widespread mortality of holm oak in open woodlands of
900 Southwestern Spain. Dendrochronologia 38, 51–60. doi:10.1016/j.dendro.2016.03.003

901 Naumann, J.C., Anderson, J.E., Young, D.R., 2008. Linking physiological responses,
902 chlorophyll fluorescence and hyperspectral imagery to detect salinity stress using the
903 physiological reflectance index in the coastal shrub, Myrica cerifera. Remote Sens.
904 Environ. 112, 3865–3875. doi:10.1016/j.rse.2008.06.004

905 North, P., 1996. Three-dimensional forest light interaction model using a Monte Carlo
906 method. IEEE Trans. Geosci. Remote Sens. 34, 946–956. doi:10.1109/36.508411

907 North, P.R.J., Rosette, J.A.B., Suárez, J.C., Los, S.O., 2010. A Monte Carlo radiative transfer
908 model of satellite waveform LiDAR. Int. J. Remote Sens. 31, 1343–1358.
909 doi:10.1080/01431160903380664

910 Pedrós, R., Moya, I., Goulas, Y., Jacquemoud, S., 2008. Chlorophyll fluorescence emission
911 spectrum inside a leaf. Photochem. Amp Photobiol. Sci. Off. J. Eur. Photochem. Assoc.
912 Eur. Soc. Photobiol. 7, 498–502. doi:10.1039/b719506k

913 Prieto-Blanco, A., North, P.R.J., Barnsley, M.J., Fox, N., 2009. Satellite-driven modelling of
914 Net Primary Productivity (NPP): Theoretical analysis. Remote Sens. Environ. 113,
915 137–147. doi:10.1016/j.rse.2008.09.002

916 Ramage, B.S., Forrestel, A.B., Moritz, M.A., O'Hara, K.L., 2012. Sudden oak death disease
917 progression across two forest types and spatial scales. J. Veg. Sci. 23, 151–163.
918 doi:10.1111/j.1654-1103.2011.01340.x

919 Roig Gómez, S., Ponce, R.A., González Sánchez, M., García del Barrio, J.M., Cañellas Rey
920 de Viñas, I., 2007. Caracterización de la dehesa española de encina y alcornoque a
921 partir del inventario forestal nacional. Cuad. Soc. Esp. Cienc. For. 163–170.

922 Rossini, M., Nedbal, L., Guanter, L., Ač, A., Alonso, L., Burkart, A., Cogliati, S., Colombo,
923 R., Damm, A., Drusch, M., Hanus, J., Janoutova, R., Julitta, T., Kokkalis, P., Moreno,
924 J., Novotny, J., Panigada, C., Pinto, F., Schickling, A., Schüttemeyer, D., Zemek, F.,
925 Rascher, U., 2015. Red and far red Sun-induced chlorophyll fluorescence as a measure
926 of plant photosynthesis. Geophys. Res. Lett. 42, 2014GL062943.
927 doi:10.1002/2014GL062943

928 Rouse, J.W., Jr., Haas, R.H., Schell, J.A., Deering, D.W., 1974. Monitoring Vegetation
929 Systems in the Great Plains with Erts. NASA Spec. Publ. 351, 309.

930 Scholander, P.F., Bradstreet, E.D., Hemmingsen, E.A., Hammel, H.T., 1965. Sap Pressure in
931 Vascular Plants. Science 148, 339–346. doi:10.1126/science.148.3668.339

932 Thayer, S.S., Björkman, O., 1990. Leaf Xanthophyll content and composition in sun and
933 shade determined by HPLC. Photosynth. Res. 23, 331–343. doi:10.1007/BF00034864

van der Tol, C., Verhoef, W., Timmermans, J., Verhoef, A., Su, Z., 2009. An integrated model of soil-canopy spectral radiances, photosynthesis, fluorescence, temperature and energy balance. Biogeosciences 6, 3109–3129. doi:10.5194/bg-6-3109-2009

Van Wittenberghe, S., Alonso, L., Verrelst, J., Hermans, I., Valcke, R., Veroustraete, F., Moreno, J., Samson, R., 2014. A field study on solar-induced chlorophyll fluorescence and pigment parameters along a vertical canopy gradient of four tree species in an urban environment. Sci. Total Environ. 466–467, 185–194. doi:10.1016/j.scitotenv.2013.07.024

Van Wittenberghe, S., Alonso, L., Verrelst, J., Moreno, J., Samson, R., 2015. Bidirectional sun-induced chlorophyll fluorescence emission is influenced by leaf structure and light scattering properties — A bottom-up approach. Remote Sens. Environ. 158, 169–179. doi:10.1016/j.rse.2014.11.012

Verhoef, W., 2004. Extension of SAIL to model solar - induced canopy fluorescence spectra. Presented at the Proceedings of the 2nd international workshop on remote sensing of vegetation fluorescence, Paris : ESA, 2004. (ESA WPP ; 242), Montreal, Canada, p. 18p.

Verrelst, J., Rivera, J.P., van der Tol, C., Magnani, F., Mohammed, G., Moreno, J., 2015. Global sensitivity analysis of the SCOPE model: What drives simulated canopy-leaving sun-induced fluorescence? Remote Sens. Environ. 166, 8–21. doi:10.1016/j.rse.2015.06.002

Verrelst, J., van der Tol, C., Magnani, F., Sabater, N., Rivera, J.P., Mohammed, G., Moreno, J., 2016. Evaluating the predictive power of sun-induced chlorophyll fluorescence to

956 estimate net photosynthesis of vegetation canopies: A SCOPE modeling study. Remote
957 Sens. Environ. 176, 139–151. doi:10.1016/j.rse.2016.01.018

958 Vilfana, N., van der Tol, C., Muller, O., Rascher, U., Verhoef , W., 2016. Fluspect-B: A
959 model for leaf fluorescence, reflectance and transmittance spectra. Remote Sens.
960 Environ. 186, 596–615. doi: 10.1016/j.rse.2016.09.017

961 Widlowski, J.-L., Taberner, M., Pinty, B., Bruniquel-Pinel, V., Disney, M., Fernandes, R.,
962 Gastellu-Etchegorry, J.-P., Gobron, N., Kuusk, A., Lavergne, T., Leblanc, S., Lewis,
963 P.E., Martin, E., Mõttus, M., North, P.R.J., Qin, W., Robustelli, M., Rochdi, N.,
964 Ruiloba, R., Soler, C., Thompson, R., Verhoef, W., Verstraete, M.M., Xie, D., 2007.
965 Third Radiation Transfer Model Intercomparison (RAMI) exercise: Documenting
966 progress in canopy reflectance models. J. Geophys. Res. Atmospheres 112, D09111.
967 doi:10.1029/2006JD007821

968 Widlowski, J.-L., Robustelli, M., Disney, M., Gastellu-Etchegorry, J.-P., Lavergne, T.,
969 Lewis, P., North, P.R.J., Pinty, B., Thompson, R., Verstraete, M.M., 2008. The RAMI
970 On-line Model Checker (ROMC): A web-based benchmarking facility for canopy
971 reflectance models. Remote Sens. Environ. 112, 1144–1150.
972 doi:10.1016/j.rse.2007.07.016

973 Widlowski, J.-L., Mio, C., Disney, M., Adams, J., Andredakis, I., Atzberger, C., Brennan, J.,
974 Busetto, L., Chelle, M., Ceccherini, G., Colombo, R., Côté, J.-F., Eenmäe, A., Essery,
975 R., Gastellu-Etchegorry, J.-P., Gobron, N., Grau, E., Haverd, V., Homolová, L., Huang,
976 H., Hunt, L., Kobayashi, H., Koetz, B., Kuusk, A., Kuusk, J., Lang, M., Lewis, P.E.,
977 Lovell, J.L., Malenovský, Z., Meroni, M., Morsdorf, F., Mõttus, M., Ni-Meister, W.,
978 Pinty, B., Rautiainen, M., Schlerf, M., Somers, B., Stuckens, J., Verstraete, M.M.,
979 Yang, W., Zhao, F., Zenone, T., 2015. The fourth phase of the radiative transfer model

intercomparison (RAMI) exercise: Actual canopy scenarios and conformity testing. Remote Sens. Environ. 169, 418–437. doi:10.1016/j.rse.2015.08.016

Zarco-Tejada, P.J., Miller, J.R., Noland, T.L., Mohammed, G.H., Sampson, P.H., 2001. Scaling-up and model inversion methods with narrowband optical indices for chlorophyll content estimation in closed forest canopies with hyperspectral data. IEEE Trans. Geosci. Remote Sens. 39, 1491–1507. doi:10.1109/36.934080

Zarco-Tejada, P., Berjon, A., Lopezlozano, R., Miller, J., Martin, P., Cachorro, V., Gonzalez, M., de Frutos, A., 2005. Assessing vineyard condition with hyperspectral indices: Leaf and canopy reflectance simulation in a row-structured discontinuous canopy. Remote Sens. Environ. 99, 271–287. doi:10.1016/j.rse.2005.09.002

Zarco-Tejada, P.J., Catalina, A., González, M.R., Martín, P., 2013a. Relationships between net photosynthesis and steady-state chlorophyll fluorescence retrieved from airborne hyperspectral imagery. Remote Sens. Environ. 136, 247–258. doi:10.1016/j.rse.2013.05.011

Zarco-Tejada, P.J., Suarez, L., Gonzalez-Dugo, V., 2013b. Spatial Resolution Effects on Chlorophyll Fluorescence Retrieval in a Heterogeneous Canopy Using Hyperspectral Imagery and Radiative Transfer Simulation. IEEE Geosci. Remote Sens. Lett. 10, 937–941. doi:10.1109/LGRS.2013.2252877

Zarco-Tejada, P.J., Morales, A., Testi, L., Villalobos, F.J., 2013c. Spatio-temporal patterns of chlorophyll fluorescence and physiological and structural indices acquired from hyperspectral imagery as compared with carbon fluxes measured with eddy covariance. Remote Sens. Environ. 133, 102–115. doi:10.1016/j.rse.2013.02.003

1002 Zarco-Tejada, P.J., González-Dugo, M.V., Fereres, E., 2016. Seasonal stability of chlorophyll
1003 fluorescence quantified from airborne hyperspectral imagery as an indicator of net
1004 photosynthesis in the context of precision agriculture. Remote Sens. Environ. 179, 89–
1005 103. doi:10.1016/j.rse.2016.03.024

1006

List of Figure captions

Fig. 1. Airborne hyperspectral flight line acquired with the micro-hyperspectral imager yielding 60 cm resolution (a), oak forest study site and tree crowns selected for the quantification of SIF (b), high resolution spectral reflectance extracted from sunlit and shadowed crown and soil components (c).

Fig. 2. Example of a 30x30 m scene (highlighted squared) of the micro-hyperspectral imagery acquired at 40 cm resolution in color-infrared (a) and sunlit and shadowed component identification of the crown on the micro-hyperspectral imagery (b). Example of a 30x30 m scene (highlighted squared) simulated with FluorFLIGHT (c) and sunlit and shadowed component identification on simulated images (d).

Fig. 3. Example of the spectral radiance extracted from the micro-hyperspectral image (a) and from FluorFLIGHT simulated radiance (L) (b) for different scene componens: sunlit crown, full crown, sunlit soil, shadowed soil and aggregated pixels (30x30 m) in the O2-A feature used for fluorescence quantification. Spectral features extracted from Fig. 2.

Fig. 4. Subplots emulating the aggregation effects due to the spatial resolution overlaid onto the micro-hyperspectral imagery acquired at 60 cm resolution (a) and a FluorFLIGHT simulated image (b), both in colour-infrared. F (FLD3) variation based on the hyperspectral image (c) and the simulated image (d) estimated from: sunlit pixels of the crown (SL crown), shadowed pixels of the crown (SW crown), full crown pixels (crown=SL+SW) and eighteen aggregated pixels from a 5x5 m window to a 100x100 m window.

Fig. 5. Simulated canopy radiance including the effects of fluorescence using the FluorFLIGHT model for a varied range of leaf area index (LAI) (0.5-4.5) (a) and fractional cover (FC) (15-65%) (b). Fluorescence quantum yield efficiency at photosystem level

(Fi=0.06). All other input parameters of the model were set using nominal values included in Table 1.

Fig. 6. Overview of the processing steps followed in the retrieval of sun-induced fluorescence (SIF) showing the input variables used for the simulations. Inputs description included in Table 1.

Fig. 7. Relationship between de-epoxidation state of the xanthophyll cycle (DEPS) (a) and water potential (b) against F (FLD3) from sunlit pixel radiance L retrieved from the hyperspectral image. Relationships between steady-state fluorescence yield (Fs) ground-data measurements of 15 oak trees and airborne-based F (FLD3) retrieved from sunlit pixel radiance (c) and 30x30 m aggregated pixels radiance (L) retrieved from the hyperspectral image (d). Trees with higher and lower level of affectation are highlighted within a dashed grey and black line respectively.

Fig. 8. Effects of forest structural variables on simulated canopy fluorescence (FLD3) as a function of LAI (0-5) at the crown level (a) and fractional cover FC (10-90%) at the canopy level (b). All other input parameters of the model were set using nominal values included in Table 1.

Fig. 9. Relationships between FluorFLIGHT simulations of canopy L obtained from sunlit crown pixels and full crowns as a function of LAI (1-4) (a). Relationships between FluorFLIGHT simulations of crown L obtained from sunlit crowns and aggregated pixels as a function of FC (10-90%) (b).

Fig. 10. Comparison of FluorFLIGHT model-based fluorescence quantum efficiency (Fi) and F (FLD3) retrieved from shaded and sunlit crown pixels, full crown pixels and aggregated pixels as a function of LAI (0-4) and FC (0-100%).

Fig 11. Relationships between the simulated FluorFLIGHT fluorescence quantum efficiency retrieved (FLD3 method) from synthetic spectra retrieved from 30x30 m aggregated pixels (a), full crown pixels (b) and sunlit crown pixels at 6.5 nm (c) and at 1 nm (d). LAI (0-4) and FC (40-60%). All other input parameters of the model were set using nominal values included in Table 1.

Fig. 12. (a) Sunlit and shadowed component identification of the crown on the micro-hyperspectral imagery. (b) SIF map showing different values between sunlit and shaded crown F (FLD3).

Fig. 13. Relationships between Fs ground-data measurements and fluorescence estimations retrievals using FluorFLIGHT applied to aggregated pixels without accounting for pixel aggregation (30x30 m aggregated pixels) and accounting for pixel aggregation (full crown pixels) with FluorFLIGHT (a) Leaf level relationship between Fs ground-data measurements and fluorescence quantum yield estimated with FluorFLIGHT (b).

Fig. 14. Fi retrieval at the crown level estimated from the 60-cm hyperspectral image using the fluorescence in-filling method F (FLD3) within the oak forest.

Table 1. Ground truth data collected and optical measurements.

Table 2. Nominal values and range of variation used in FluorFLIGHT simulation analysis based on field data measurements.

Table 3. Correlation coefficient R between steady-state fluorescence yield (Fs), de-epoxidation state of the xanthophyll cycle (DEPS) and water potential (ψ) and crown-based spectral vegetation indices, including structural and physiological vegetation indices.